Chinese Journal of
POLYMER SCIENCE

RESEARCH ARTICLE

https://doi.org/10.1007/s10118-026-3758-7
Chinese J. Polym. Sci.

Microscopic Insights into the Mechanism of Microporous Polymer Membrane Preparation by Non-solvent Induced Phase Separation: a Molecular Dynamics Simulation Study

Ji-Tao Liu[a,b*], Yue-Ying Sun[a,b], Xin-Ran Dai[a,b], Zhi-Hao Zong[a], Shuai Li[a,b], Yan-Chen Li[a,b], and Chun-Sheng Li[a*]

[a] *School of Chemistry and Chemical Engineering, University of Jinan, Jinan 250022, China*
[b] *Shandong Provincial Key Laboratory of Extreme Environment-tolerant Specialty Chemicals School of Chemistry and Chemical Engineering, University of Jinan, Jinan 250022, China*

Electronic Supplementary Information

Abstract Despite extensive research, understanding the formation process of microporous polymer membranes remains an open question. Despite computational advances, all-atomic mechanistic studies of phase separation remain challenging. This study employed all-atom molecular dynamics (MD) simulations to investigate the non-solvent-induced phase separation (NIPS) process in poly(vinylidene fluoride) membrane formation. The simulated microstructure was consistent with that of the experimental ultrafiltration membranes, both exhibiting cylindrical through-pores with well-defined pore walls and symmetrically connected structures. MD simulations further reveal key parametric effects: increasing the polymer concentration reduces the phase separation rate, with the pore volume decreasing to 50.29% of the initial value at four times the original concentration. Conversely, increasing the system temperature accelerated phase separation, with the pore volume reaching 111.23% of the original value at a 60 K temperature increase. The analysis of the interaction energy, diffusion coefficient, and atomic concentration provided mechanistic insights into these observations. These MD simulations enabled atomic-level visualization of the NIPS process, capturing intermediate states that are difficult to observe in conventional experiments and elucidating the formation mechanism of microporous polymer membranes. This not only provides a theoretical basis for preparing highly permeable, highly selective microporous polymer membranes but also offers technical support for optimizing membrane fabrication processes.

Keywords Molecular dynamics simulation; Non-solvent induced phase separation; Polymer membrane; Poly(vinylidene fluoride)

Citation: Liu, J. T.; Sun, Y. Y.; Dai, X. R.; Zong, Z. H.; Li, S.; Li, Y. C.; Li, C. S. Microscopic insights into the mechanism of microporous polymer membrane preparation by non-solvent induced phase separation: a molecular dynamics simulation study. *Chinese J. Polym. Sci.* https://doi.org/10.1007/s10118-026-3758-7

INTRODUCTION

With the rapid development of the technology industry, polymer membranes have found widespread applications in key sectors such as energy, environmental protection, and healthcare[1–5] owing to their unique performance advantages, making them one of the core materials driving industrial upgrading. Membrane separation technology is increasingly demonstrating its strategic value as an important branch of modern material science. Among the various membrane preparation processes, the non-solvent induced phase separation (NIPS) method has become the mainstream technology for the industrial production of microporous polymer membranes owing to its simple operation, strong controllability, and wide applicability.[6,7] The essence of this method is that the homogeneous polymer solution undergoes phase separation due to different solubilities, forming a biphasic system consisting of a polymer-rich phase and a polymer-poor phase. The polymer-rich phase solidifies to form the main framework of the microporous membrane, whereas the polymer-poor phase forms functionally specific microporous structures after non-solvent removal.[8,9] This essentially embodies a cross-scale regulatory logic from microscopic molecular behavior to macroscopic membrane structure, providing a theoretical foundation for the design of functional membrane materials. However, traditional theoretical analyses alone and mere experimental research are insufficient to reveal this complex physical process. The increasingly mature numerical simulation technology has become an important means of understanding and investigating the behavior of polymer NIPS.[10]

Computer simulation is an important method for studying the formation process of microporous polymer membranes, and analyzing the formation mechanism of complex three-dimensional porous structures is a current research hotspot.

* Corresponding authors, E-mail: chm_liujt@ujn.edu.cn (J.T.L.)
E-mail: chm_lics@ujn.edu.cn (C.S.L.)
Received April 1, 2026; Accepted May 27, 2026; Published online September 20, 2026

© Chinese Chemical Society
Institute of Chemistry, Chinese Academy of Sciences

Cervellere *et al*.[11] developed a phase-field model to simulate the formation of porous polymer membranes by using NIPS. The research object was a polyethersulfone/*N*-methylpyrrolidone/water mixture. To verify the predictive ability of the model, the concentration of *N*-methylpyrrolidone in the coagulation bath was varied and compared with the experimental results. The cross-sectional pore morphologies and pore sizes of the membranes formed by NIPS were evaluated using two-dimensional and three-dimensional simulations. The membranes were prepared experimentally and compared with the simulation results, revealing a consistent dependence of pore morphology on the composition of the coagulation bath. Blagojevic *et al*.[12] employed a single, highly coarse-grained model to investigate the sequence of evaporation-induced self-assembly and nonsolvent-induced phase separation processes. Asymmetric copolymer microporous membranes were fabricated on Si wafers. The effects of different thermodynamic and kinetic properties on the formation and inhibition of the membrane structures are discussed. Cervellere *et al*.[13] proposed a phase-field model for thermally induced phase separation in polymer solutions, and calibrated it for a poly(vinylidene fluoride)/diphenyl carbonate system. Computer simulations were conducted for isotropic and anisotropic quenching processes. The size and connectivity of the pore structures were analyzed at different polymer volume fractions and quenching rates. In the anisotropic quenching simulations, dense crust formation was observed. Furthermore, it was found that crust thickness depends on the temperature of the water and thermal conductivity of the polymer solution. The above computer simulations, based on phase-field or coarse-grained scales, elucidate the phase separation process and bridge the gap between theory and experiment.

The aforementioned simulations of phase separation behavior primarily remain at the macroscopic and mesoscopic scales, whereas the evolution of polymer structures at the microscopic scale remains unclear. Therefore, it is necessary to investigate the mechanism of the formation of polymer microporous membranes at the atomic scale. Liu *et al*.[14] employed molecular dynamics (MD) simulations to investigate the influence of the polymer structure on phosphate distribution within polyarylpyrimidine membranes. The results indicate that during phase separation, both the electron localization and density of the acid-loving groups within the polymer affect the phosphate distribution. Strong electron localization in acid-loving groups leads to phosphate aggregation around these groups, whereas phenyl groups exhibit reduced attraction to phosphates, thereby promoting phase separation. Theodorakopoulos *et al*.[15] investigated the formation of polyimide films during NIPS using MD simulations. They compared two organic solvent systems, *N*-methylpyrrolidone and γ-butyrolactone. The porous polymer structures formed by both solvents were similar; however, the pore size distribution of the porous structure prepared using the γ-butyrolactone solvent system was slightly narrower. Additionally, the influence of polymer concentration on early stage membrane morphology was examined. Increasing the polymer concentration reduces the solvent-accessible surface area and porosity, leading to the formation of more solid structures. The aforementioned MD simulations of NIPS behavior provide a reference for investigating the mechanism of microporous polymer membrane formation. However, these simulations lack investigations into the motion and evolution of polymer chains during phase separation as well as studies on material properties and environmental factors. Therefore, employing the MD method to study NIPS behavior in the context of microporous polymer membrane formation has significant theoretical value and engineering importance.

In this work, we conducted MD simulations and experimental studies on NIPS behavior during the formation of microporous polymer membranes using poly(vinylidene fluoride)/*N*,*N*-dimethylacetamide/water as the research subjects. The motion of poly(vinylidene fluoride) (PVDF) molecular chains and the formation mechanism of micropores during NIPS were investigated at the microscopic level, with a particular focus on the effects of polymer concentration and system temperature on the membrane formation process and microscopic morphology. By integrating MD simulations and experimental results, this study reveals the evolution mechanism of NIPS behavior, providing theoretical guidance for optimizing the process parameters and product structuring in microporous polymer membrane fabrication.

METHODOLOGY AND SIMULATION DETAILS

NIPS Process

The primary cause of NIPS behavior is the rapid and drastic decrease in polymer solubility due to solvent-nonsolvent exchange, leading to phase separation, as illustrated in Fig. 1. When a homogeneous system formed by dissolving the polymer in a solvent is placed in a non-solvent, rapid solvent-nonsolvent exchange occurs, with the non-solvent penetrating the polymer. Because of the extremely low solubility of the polymer in the nonsolvent, the molecular chains aggregate and precipitate, forming a polymer-rich phase; water molecules gather in the pores to form a polymer-poor phase. After drying, water molecules (polymer-poor phase) were removed from the pores, and the polymer-rich phase resulting from phase separation constituted the microporous membrane skeleton.

Models

The process of polymer precipitation in nonsolvents is central to NIPS behavior, making it essential to conduct in-depth studies on the interactions between polymers and nonsolvents. This experiment employed MD simulation to uniformly disperse polymers in solvents, followed by solvent replacement with non-solvents to establish an initial model for phase separation. The initial model was constructed using the Materials Studio software through the following steps. Initially, a PVDF repeat unit was created, and a PVDF molecular chain with a polymerization degree of 1000 was obtained using this repeating unit. Subsequently, the PVDF molecular chain and *N*,*N*-dimethylacetamide (DMAc) were uniformly dispersed within a box (200 Å × 200 Å ×100 Å) at a specific ratio, yielding a homogeneous system. Finally, DMAc in the homogeneous system was replaced with water molecules to obtain the blend configuration, which served as the initial model for the phase separation process MD simulation. The modeling process is illustrated in Fig. 2. The modeling approach that directly replaces DMAc molecules with water

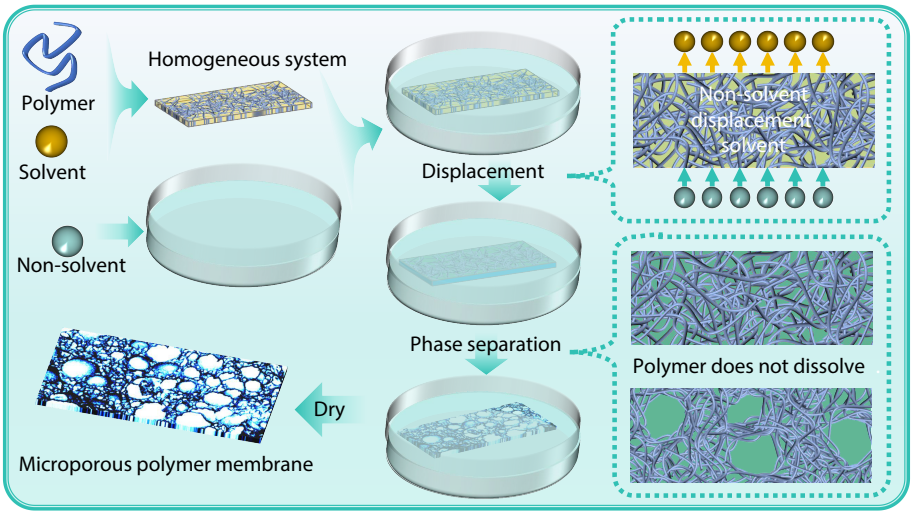


Fig. 1 Schematic diagram illustrating the principle of the NIPS process.

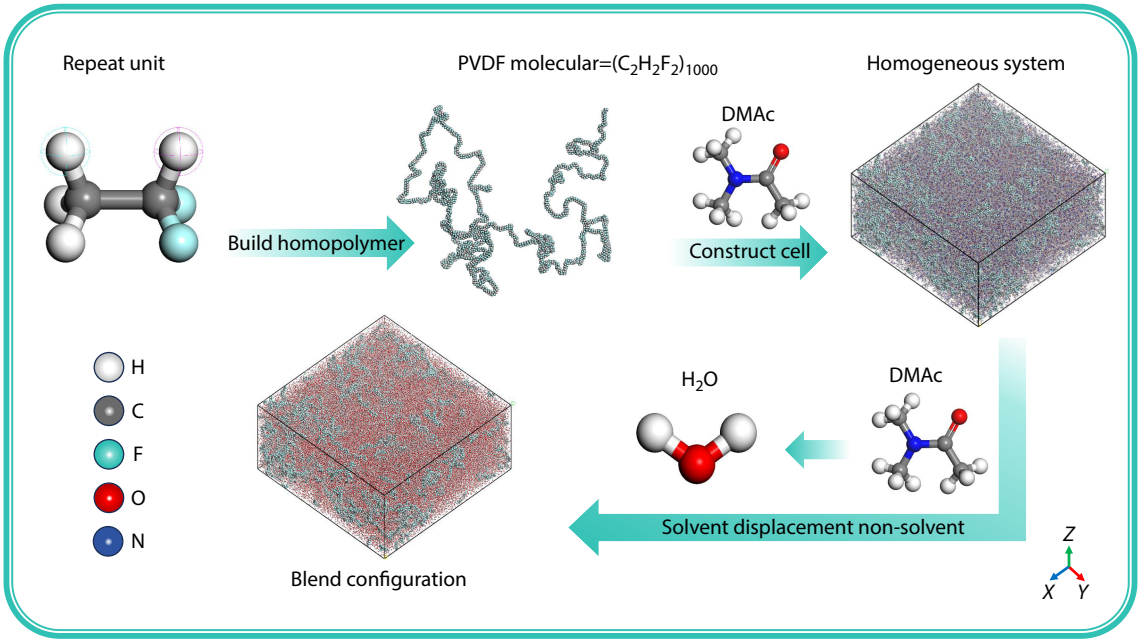


Fig. 2 Schematic diagram of constructing an initial model for the NIPS process.

molecules bypasses the solvent-non-solvent exchange process during the NIPS procedure. This method is a time-saving and simplified modeling approach. As such, it may have influenced the initial phase separation process. Because this study focuses on the phase separation behavior driven by the incompatibility between PVDF and water, as well as the pores formed after phase separation, a simplified modeling approach is appropriate for this study.

To investigate the effects of PVDF concentration and system temperature on phase separation during the NIPS process, seven MD simulation models were constructed. Four of these models contained varying numbers of molecular chains to examine the influence of PVDF concentration on phase separation. Within identical-volume boxes, the number of PVDF chains was set to 5, 10, 15, and 20 and designated as PVDF-5, PVDF-10, PVDF-15, and PVDF-20, respectively. Additionally, for the PVDF-10 system, three temperatures were selected to investigate the effect of system temperature on phase separation: 273, 298, and 333 K. Specifically, a low temperature (273 K) close to the freezing point of water, a standard temperature (298 K) representing room temperature, and a high temperature (333 K) used to prepare the casting solution in the experiments were purposefully selected. Table 1 lists the composition of the model.

Simulation Process

All MD simulations were performed using a large-scale atomic/molecular massive parallel simulator (LAMMPS).[16] The Polymer Consistent Force Field (PCFF)[17–19] was employed to describe system interactions, primarily designed for polymers[20–22] but also applicable to simulations involving small molecules[23] such as water. In this study, the PCFF was employed to describe all atomic interactions, including those in-

Table 1 Composition of the initial model simulating the NIPS process.

Name	Temperature (K)	Number of PVDF molecules $(C_2H_2F_2)_{1000}$	Number of DMAc molecules	Number of H_2O molecules	PVDF concentration (wt%)
PVDF-5	298	5	23973	112185	15.33
PVDF-10	298	10	20298	98176	26.58
PVDF-15	298	15	16625	80398	39.87
PVDF-20	298	20	12948	62649	53.16
273 K	273	10	20298	98176	26.58
298 K	298	10	20298	98176	26.58
333 K	333	10	20298	98176	26.58

volving water molecules. The PCFF native water model was used for the water molecules. To verify its suitability for simulating the NIPS process, benchmark simulations of the water molecules were performed at 298 K and 101.325 kPa. The simulated density was 0.986 g/cm^3 (experimental value: 0.997 g/cm^3), and the diffusion coefficient was 5.3×10^{-9} m^2/s (reported value in the literature: 5.28×10^{-9} m^2/s[24,25]). The simulated density value agrees closely with the experimental value, with a standard deviation of only 1.1%, confirming that the PCFF natural water model can accurately reproduce the thermodynamic properties of water. The simulated value of the self-diffusion coefficient is extremely close to the literature-reported value, with a standard deviation of only 0.4%, further validating the reliability of this model in describing the hydrodynamic behavior of water. In summary, the PCFF natural water model was suitable for the NIPS simulations in this study.

The PCFF belongs to the ab initio consistent force-field family, which also includes the CFF91, CFF, and COMPASS force fields. The energy calculated using the PCFF consists of the following five components:

$$E_{\text{total}} = E_{\text{bond}} + E_{\text{angle}} + E_{\text{dihedral}} + E_{\text{improper}} + E_{\text{non-bonded}} \quad (1)$$

where the sum of bond (E_{bond}), angle (E_{angle}), dihedral (E_{dihedral}), and improper (E_{improper}) terms denote the bonded interactions, and non-bonded ($E_{\text{non-bonded}}$) terms represent the non-bonded interactions. The bonded and non-bonded interactions are equal to the total energy (E_{total}).

Utilizing 9-6 Lennard-Jones potential[26] to calculate the non-bonded interactions.

$$E_{\text{non-bonded}} = LJ(\gamma) = \varepsilon\left[2(\sigma/\gamma)^9 - 3(\sigma/\gamma)^6\right], \gamma < \gamma_c \quad (2)$$

where σ is the equilibrium distance, ε is the equilibrium well depth, and the cutoff distance r_c is set to 10 Å. For the interaction parameters between different types of atoms,[27] both σ and ε are calculated based on the commonly used Lorentz-Berthelot mixing rule:

$$\sigma_{AB} = 0.5\,(\sigma_{AA} + \sigma_{BB}) \quad (3)$$

$$\varepsilon_{AB} = \sqrt{\varepsilon_{AA}\varepsilon_{BB}} \quad (4)$$

in the formula, A and B are different types of atoms.

The entire simulation process consisted of two parts: energy minimization and MD simulations. First, energy minimization is performed using the conjugate gradient method.[22,28] This step eliminates unreasonable phenomena caused by excessive system energy resulting from atoms being too close in space. Subsequently, an MD simulation of the NIPS process was conducted by utilizing the temperature and pressure stability of the NPT collective control system. The simulated system exhibited periodicity in all the three dimensions. The time step was set to 1 fs, with a frame of kinetic results output every 5×10^4 steps for the analysis.

Unless otherwise specified, the final 1 fs of each trajectory was used for the analysis, with one frame captured every 50 ps. The Open Visualization Tool (OVITO)[29] was employed for model visualization and post-processing operations. In this study, repeated simulations were conducted on a single system and the results obtained were nearly identical. This is because the large system size and the use of average data output methods (fixed ave/time) enhanced the stability of the data in this study. At the same time, this also demonstrates the stability of the simulation trajectories in this study.

Data Analysis

Interaction energy and solubility coefficient

Compatibility between PVDF and water is a decisive factor in the NIPS process. The intermolecular forces determine the compatibility of different substances.[30] The interaction energy calculated in MD simulations can dynamically capture changes in the interactions between materials. This enabled the prediction of the variation in PVDF-water compatibility, further evaluating the degree of phase separation. The interaction energy calculation process is expressed as follows:

$$E_{\text{interaction}} = E_{\text{total}} - E_{\text{intramolecular}} \quad (5)$$

where E_{total} and $E_{\text{intramolecular}}$ refer to the total energy of the system and the energy of the intramolecular interactions (bond lengths, bond angles, dihedral angles, *etc.*).

During the NIPS process, both the PVDF molecular chains and water undergo aggregation. The cohesive energy can be used to compare the binding forces between molecular chains.[31] The cohesive energy per unit volume was defined as the cohesive energy density. The solubility parameters were calculated as follows:

$$E_{\text{coh}} = -E_{\text{interaction}} \quad (6)$$

$$\text{CED} = \frac{E_{\text{coh}}}{V} \quad (7)$$

$$\delta = \sqrt{\text{CED}} \quad (8)$$

where E_{coh} is the cohesive energy, CED is the cohesive energy density, V is volume, and δ is a solubility parameter.

In addition, the Flory-Huggins parameter χ is one of the key methods for directly calculating thermodynamic parameters related to phase separation.[32,33] The calculation process is described by the following equation:

$$\chi = V_{solvent}\left(\delta_{polymer} - \delta_{solvent}\right)^2 / (R \cdot T) \quad (9)$$

where $V_{solvent}$ is the molar volume of the solvent, R is the gas constant, and T is the system temperature.

Concentration analysis of PVDF in the X direction

To investigate the motion of the PVDF molecular chains during NIPS, the atomic concentration distribution along the *X*-direction was quantified. The coordinates of all PVDF atoms in the system are output. The system was partitioned into 20 regions along the *X*-axis, and the total number of PVDF atoms within each region was counted.

Analysis of fluorine atom counts in dynamic regions

During the NIPS process, the PVDF molecular chains aggregate to form a microporous membrane framework. The degree of PVDF molecular chain aggregation was investigated by calculating the number of fluorine atoms in a specific region. The fluorine atom in the system served as the study subject, with a spherical region centered on this atom defined to count the number of fluorine atoms within it. Note that the position of the spherical region shifts with atomic movement during the phase separation. To mitigate the impact of specific atomic locations, ten atoms were randomly selected from the membrane skeleton as test subjects. The average number of fluorine atoms surrounding these atoms was calculated and used as the basis for analysis.

Analysis of molecular chain mobility

During NIPS, the atoms within the system undergo continuous motion, ultimately leading to enrichment or separation. To evaluate the mobility of the PVDF molecular chains during NIPS, the mean square displacement (MSD) and the diffusion coefficient (D) were calculated.[31,34] The MSD is a function of time, which describes the average displacement of atoms over time:

$$\mathrm{MSD}(t) = \left\langle \left| r_i(t) - r_i(0) \right|^2 \right\rangle \quad (10)$$

where t is the counting time, $r_i(0)$ is the starting position of the center of molecule i, $r_i(t)$ is the position of molecule i at the central moment t and the brackets are the mean values.

The diffusion ability of a molecular chain can be determined by calculating D[35,36] from the slope of the MSD curve:

$$D = \left(\frac{1}{6}\right) \times \lim_{t\to\infty} \left(\frac{\mathrm{d}}{\mathrm{d}t}\right) \mathrm{MSD}(t) \quad (11)$$

To visually observe the mobility of the molecular chains, the atomic displacements were analyzed using OVITO post-processing and plotted as atomic displacement contour plots.

Density distribution cloud map

Conducting a density distribution analysis of the results after NIPS is an effective method for evaluating the degree of phase separation. The system was divided into 100 segments along the *X*- and *Y*-directions. Along the *Z*-axis, the system was partitioned into 1×10^4 grid cells. The number of fluorine atoms within each cell was counted, and PVDF and water atoms were color-coded to generate an atomic density cloud map.

Pore volume analysis

The homogeneous system underwent spontaneous separation *via* NIPS to form polymer-rich and polymer-poor phases. Water molecules were removed from the polymer-poor phase through drying, forming a porous membrane framework in the polymer-rich phase. The pore volume is a critical parameter that affects the permeability, mechanical strength, and functional applications of porous membranes.[37–39] Use OVITO software to identify surface atoms and visually represent pore sizes and morphologies. The pore surface and cross-sectional images were color-coded with distinct shades to generate the pore morphology maps. These pore morphology maps were processed using OVITO to calculate the pore volume of the porous membranes.

Experiments

Materials

PVDF (FR-904) with a molecular weight of 6×10^5 g/mol was obtained from Shanghai 3F New Materials Co., Ltd. (China) and its molecular weight is 6×10^5 g/mol. *N*,*N*-dimethylacetamide (DMAc, >99.5%) was purchased from Tianjin Fuyu Fine Chemical Co., Ltd. (China). Laboratory water was prepared using deionized water produced in the laboratory.

PVDF membrane prepared via the NIPS process

Dissolve PVDF in DMAc and stirred at a constant speed for 10 h at 60 °C to obtain a uniform PVDF solution. The PVDF solution was allowed to stand at the same temperature for 12 h to dissipate bubbles. The liquid was cast onto a glass plate by using a casting knife with a gap height of 200 μm. Transfer the nascent membranes to a 25 °C water bath to obtain solidified PVDF membranes through the NIPS process. After spontaneous delamination from the glass plate, the PVDF membranes were stored in flowing deionized water to remove eluates. The membranes were dried to remove residual moisture, yielding PVDF ultrafiltration membranes for filtration applications.

PVDF membrane characterization

The morphology of the PVDF membrane, including its surface and cross-sectional structure, was observed using a field-emission scanning electron microscope (FESEM, Gemini300, Carl Zeiss AG, Germany). Cross-sections of the membrane were prepared using liquid nitrogen brittle fracture. All samples underwent gold sputtering before testing to enhance their conductivity.

The porosity of the membrane was determined using wet and dry weighing methods. The specific procedure was as follows: the membrane was cut into samples of equal area; after wiping the surface moisture with filter paper, the mass was recorded as W_w; the samples were placed in a vacuum oven and dried at 60 °C for 24 h, and the mass was recorded again as W_d. The porosity was calculated as follows:

$$\varepsilon = (W_w - W_d) / (\rho_w A \delta_0) \quad (12)$$

where ε is the porosity of the separation membrane; W_w and W_d are the wet and dry weights of the separation membrane, respectively; A is the membrane area; δ_0 is the membrane thickness; and ρ_w is the density of pure water.

RESULTS AND DISCUSSION

Non-solvent Induced Phase Separation Process

To provide a more complete thermodynamic description of the driving forces behind the phase separation, we estimated the Flory-Huggins interaction parameter χ for the PVDF-water system. The core of Flory-Huggins theory describes the change in the mixing free energy (ΔG_{mix}) between the polymer and the solvent. The Flory-Huggins parameter χ incorporates both en-

thalpy and entropy contributions, thereby providing a more comprehensive reflection of the compatibility between the polymer and the solvent. According to Flory-Huggins theory, when χ>0.5, the polymer and solvent are considered incompatible. The calculated value of χ=1.98 > 0.5, providing quantitative thermodynamic confirmation of the incompatibility between PVDF and water. This result provides direct thermodynamic evidence for the occurrence of phase separation during the NIPS process. It is precisely this thermodynamic incompatibility that drives PVDF molecular chains to aggregate and precipitate from the solution, forming a polymer-rich phase, while water molecules aggregate to form a polymer-poor phase, ultimately resulting in a microporous structure.

The essence of the NIPS process lies in the extremely low solubility of polymers in non-solvents, which enables the polymer to precipitate and solidify. The interaction between the PVDF and water molecules drives this process. The evolution of the interaction energies over time and snapshots of the phase separation process are shown in Fig. 3. Simulations revealed extremely high interaction energies in the PVDF-H_2O system at the initial moment, which monotonically decreased as the NIPS process progressed. These data indicate that the interaction between PVDF and water was most intense during the early stages of phase separation and rapidly reached a relatively stable equilibrium state over time. The decreasing trend in the interaction energies over time is primarily attributed to the thermodynamic and kinetic processes of NIPS.

During the first stage of phase separation (0–1 ns), a large number of water molecules instantaneously flood the polymer solution, placing the system in a highly non-equilibrium state. The initial high interaction energy stems from the instantaneous, extensive contact between water and the PVDF chains; the subsequent decrease is due to the aggregation of the PVDF chains, which reduces the contact area. Additionally, strong dipole-dipole interactions and hydrogen bonding between the water molecules and fluorine atoms on the PVDF chains are also likely contributors.[40–42]

During the second stage of phase separation (1–3 ns), the PVDF molecular chains aggregate and solidify into a film. This encapsulates most of the polymer chains within the film, reducing their surface area in direct contact with water molecules. Consequently, the number of PVDF segments capable of direct interactions with water molecules decreased significantly, leading to a rapid decline in the interaction energy.

In the final stage of phase separation (3–5 ns), the evolution of the system structure slows down, and the membrane morphology is established. At this stage, the interactions primarily occur at the membrane interface. Consequently, the rate of change of the interaction energy decreases significantly and gradually approaches a dynamic equilibrium value. This indicates that the NIPS process was essentially complete, and the interaction between PVDF and water reached a relatively stable state.

In summary, the variation in interaction energy clearly reflects the NIPS process. This process encompasses the entire evolution from the initial vigorous motion to polymer solidification, culminating in the transition from a non-equilibrium state to a metastable state.

During the NIPS process, PVDF and water molecules, which were originally intermingled, underwent phase restructuring and aggregated to form polymer-rich and polymer-poor phases, respectively. To quantitatively track this process, Fig. 3

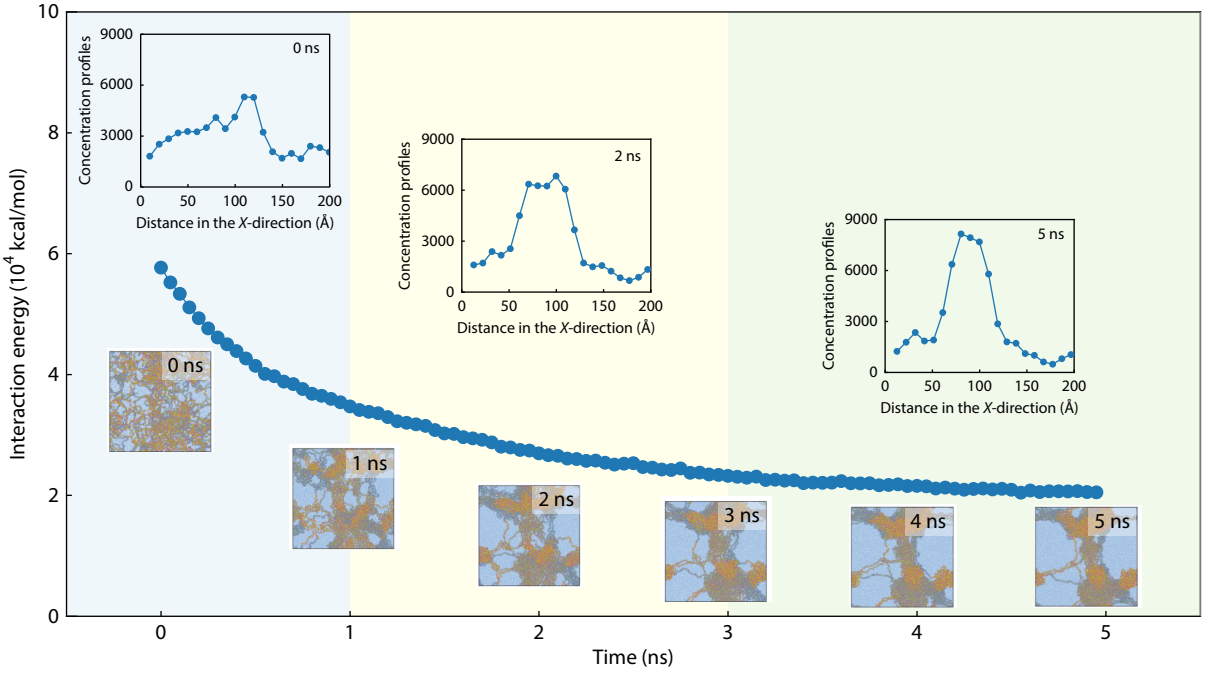


Fig. 3 Time-dependent interaction energy curves between PVDF chains and water molecules during the NIPS process at 298 K for a system containing 10 PVDF chains with a polymerization degree of 1000. It also includes concentration distribution curves of the PVDF chain at 0, 2 and 5 ns, along with snapshots at 0, 1, 2, 3, 4 and 5 ns.

https://doi.org/10.1007/s10118-026-3758-7

displays the atomic concentration distribution curves of PVDF along the *X*-direction at 0, 2, and 5 ns. In the initial state, the PVDF molecular chains were uniformly dispersed, resulting in a relatively flat concentration distribution curve along the *X*-direction. As the NIPS process progressed, the concentration distribution curve exhibited significant fluctuations and formed characteristic peaks. Simultaneously, the aggregation behavior of the PVDF molecular chains can be directly observed in the corresponding simulation snapshots. Taking the 5 ns time point when phase separation occurs as an example, the concentration curve displays a sharp peak. This correlates with the distinct phase separation morphology visible in the snapshot, collectively indicating that the mixed configuration was disrupted and separated into a water phase and PVDF phase. The following sections provide detailed analyses of the kinetic evolution and outcomes of NIPS.

During NIPS, the system undergoes phase separation from a homogeneous state to a two-phase state. During this process, the PVDF molecular chains and water molecules aggregate separately. The aggregation of the PVDF molecular chains was verified by counting the number of fluorine atoms within a specific region, as shown in Fig. 4. In the blend configuration, water molecules were uniformly dispersed within the voids of the PVDF chains, resulting in a low number of fluorine atoms within the spherical region at the initial state. As NIPS progressed, the number of fluorine atoms increased and then stabilized, confirming the aggregation of PVDF chains during phase separation. In the later stages of the NIPS process, the number of fluorine atoms within the spherical region ceases to increase, indicating that a stable condensed-phase structure is gradually formed through phase separation. The error bars in Fig. 4 reveal larger atomic number errors between 1–3 ns. This is attributed to the significant variation in atomic motion speeds at different positions, leading to different phase separation rates and consequently larger measurement errors.

The rich polymer phase formed by NIPS undergoes drying to create microporous polymer membranes, which are widely applied in water treatment,[43,44] gas separation,[45,46] battery separators,[47] and other applications. Their tunable pore size, high specific surface area, chemical designability, and mechanical flexibility enable their broad utilization across multiple domains.[10] This study employed an all-atom MD simulation method to model the microscopic mechanisms of the NIPS process, with a particular focus on the pore structure formed during phase separation. OVITO post-processing was used to extract the pore volume evolution during the NIPS. Fig. 5 displays the pore volume evolution curve during NIPS for a system containing 10 PVDF molecular chains with a polymerization degree of 1000 at 298 K. Within the initial 0–1 ns of phase separation, the pore volume exhibits a linear increase. Within the 1–3 ns stage, phase separation continued at a slower rate, with the pore volume rising parabolically. Between 3–5 ns, the pore volume stabilized as phase separation formed a stable porous structure. Combining the pore volume curve with simulation snapshot analysis reveals that the NIPS process comprises three distinct stages. First, phase separation rapidly forms multiple small pores. Second, these small pores rapidly increased in volume and coalesced into interconnected pores. Finally, the interconnected pores slowly expand, and the pore volume continues to increase until phase separation is complete.

The key to determining whether the simulation of the NIPS process is credible lies in whether the porous structure formed by the numerical study matches the porous structure formed by the actual experiment. Therefore, the microstructure formed by the molecular simulation was compared with that of the experimentally synthesized PVDF ultrafiltration

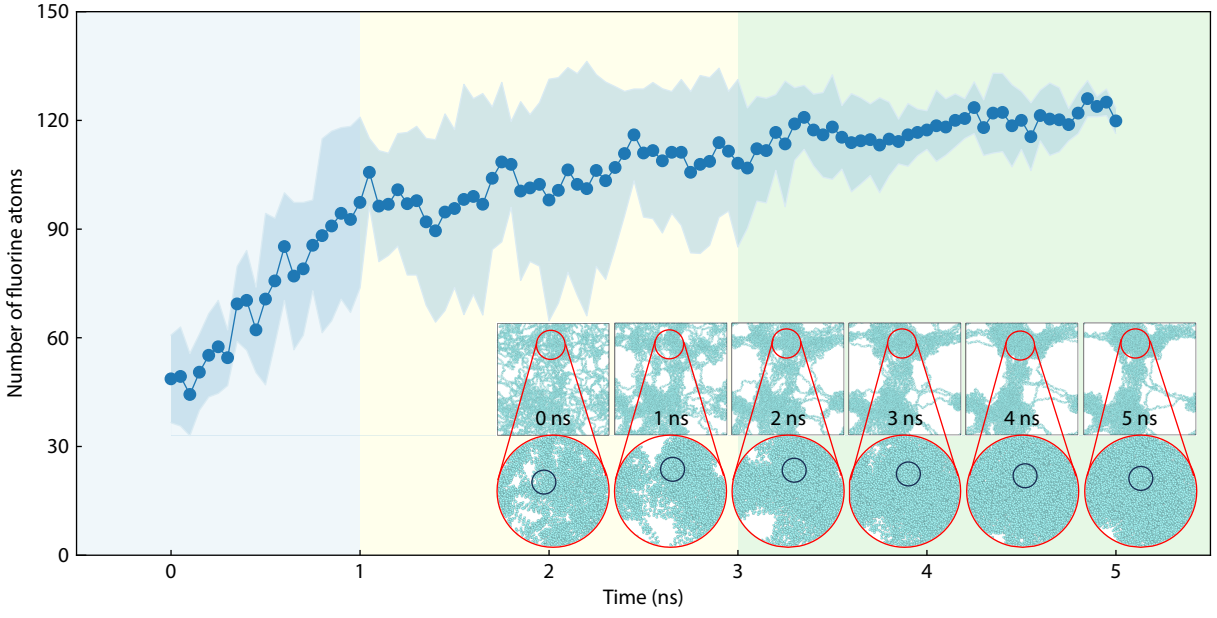


Fig. 4 Fluorine atom count curve within the dynamic spherical region during the NIPS process at 298 K for a system containing 10 PVDF molecular chains with a polymerization degree of 1000, along with snapshots of the spherical region at 0, 1, 2, 3, 4 and 5 ns. (Ten fluorine atoms in the polymer enrichment phase were selected as the subjects, and the number of other fluorine atoms within a 10 Å radius of them was calculated.)

https://doi.org/10.1007/s10118-026-3758-7

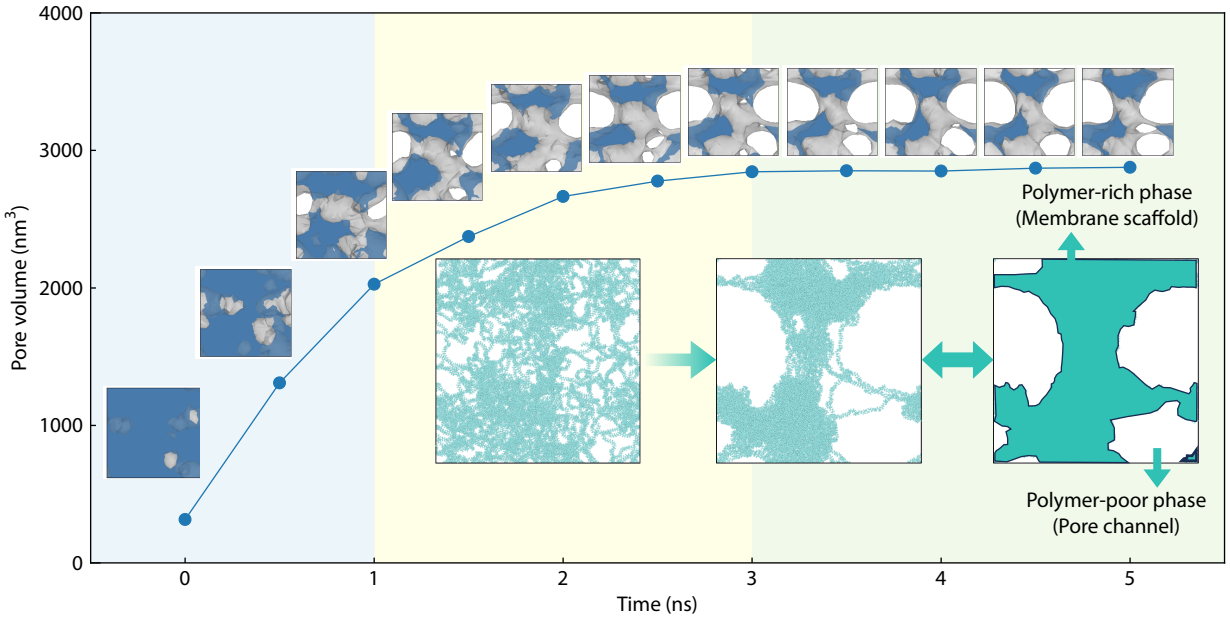


Fig. 5 Pore volume change curve and pore morphology snapshot during the NIPS process at 298 K for a system containing 10 PVDF molecular chains with a polymerization degree of 1000. And the schematic diagram illustrating the distinction between the polymer-rich phase (membrane scaffold) and the polymer-poor phase (pore channel).

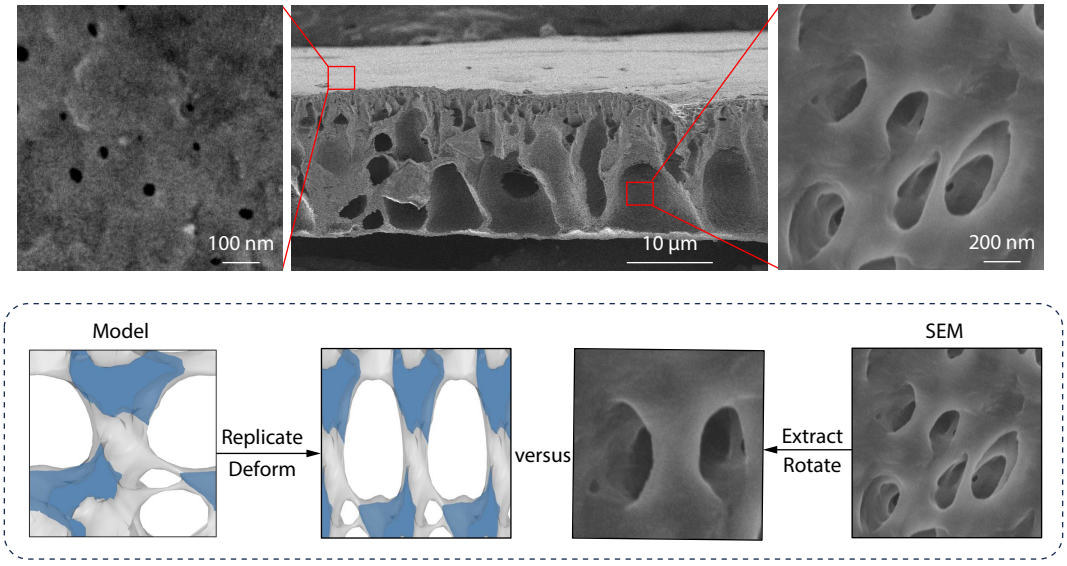


Fig. 6 SEM images of the PVDF membrane surface (the separation layer), cross-section, fracture surface (the support layer) and comparison of the SEM image and the simulated microstructure.

membrane. The laboratory-prepared PVDF ultrafiltration membrane comprised two key structural layers: a separation layer and a support layer (Fig. 6). The separation layer, located on the surface skin of the PVDF membrane, functions as a sieve and directly participates in the retention and separation of impurities. The support layer was thicker than the separation layer, featuring a loose, porous structure containing numerous through-pores. This dual-layer design enables PVDF ultrafiltration membranes to achieve efficient and long-lasting separation in applications such as wastewater treatment, food concentration, and biopharmaceutical production.[48,49]

To compare the molecular simulations with the experimental results, the final frame snapshot of the simulated NIPS process was compared with the electron micrograph obtained experimentally. The viewing angle of the SEM images distorted the three-dimensional pore structure. To standardize the viewing angle, operations such as Replicate and Extract were applied to both the snapshot and the electron microscope image in Fig. 6. The NIPS process was simulated using MD, and the resulting pore structure was similar to the pore morphology observed using SEM. Both methods yielded clear cylindrical through pores with distinct pore walls. The simulation reproduced the key topological structures observed experimentally, including symmetric pore morphology and connectivity. It can be demonstrated that the PCFF force field

employed in the simulations effectively describes the interactions between PVDF molecular chains and water molecules. The simulation parameters were appropriately configured to capture the pore structure under experimental conditions. This comparative analysis not only demonstrates the reliability of the simulation methodology but also provides a foundation for subsequent predictive studies based on this process.

The comparison between the MD simulation results and SEM images is qualitative and suffers from a scale mismatch. Therefore, a quantitative parameter of porosity was introduced to enable a more objective comparison. In this study, the porosity extracted from the simulation was compared to the experimentally calculated porosity, as listed in Table 2. There was a deviation of approximately 6.59 percentage points between the simulated porosity (79.05%) and the experimental porosity (72.46%), with a relative error of approximately 9.10%. This relative error falls within the typical error range (5%–15%) for all-atom MD simulations, indicating that the simulation is quantitatively reliable.

Table 2 Comparison of membrane porosity (simulation versus experiment).

	Porosity (%)	Deviation
Simulation (PVDF-10)	79.05	0.31
Experiment	72.46	1.47

In summary, the simulations successfully reproduced the pore morphology observed in the experiments, demonstrating the qualitative reliability of this study; the errors fell within an acceptable range, providing quantitative reference values; and the simulations filled the gaps in the dynamic processes and molecular mechanisms that could not be observed experimentally. Therefore, the MD simulation method used in this study is reliable and explanatory, capable of providing atomic-level theoretical support for the formation mechanism of microporous structures during the NIPS process and offering clear guidance for the optimization of experimental processes.

Concentration Dependence

To investigate the effect of PVDF concentration on the NIPS process, the evolution and aggregation of PVDF molecular chains were studied across different concentration systems. After masking the water molecules in the system, the PVDF molecular chains were labeled with distinct colors. Snapshots of the NIPS process at 298 K for the systems with different PVDF concentrations are shown in Fig. 7. In the initial model, the molecular chains in the systems of varying concentrations exhibited a uniform distribution and intertwined states. During the early stage of phase separation, nearby molecular chains aggregate to form small PVDF clusters, initially creating multiple micropores. In the intermediate stage, aggregated PVDF chains are attracted to and tightly bonded with each other, causing existing micropores to coalesce into larger pores. From this point onward, the number of pores remains largely constant. In the late stage, the continuous thermal motion of the PVDF chains further tightened their bonds, causing the formed through-holes to enlarge gradually until the pore size stabilized. Summarizing the phase separation process across different concentrations reveals that the size of the pores formed after NIPS decreased with increasing PVDF concentration.

The interaction energy between water and PVDF was used as a quantitative indicator to calculate the driving force for the phase separation. MD simulations were conducted to compute the interaction energy between the PVDF molecu-

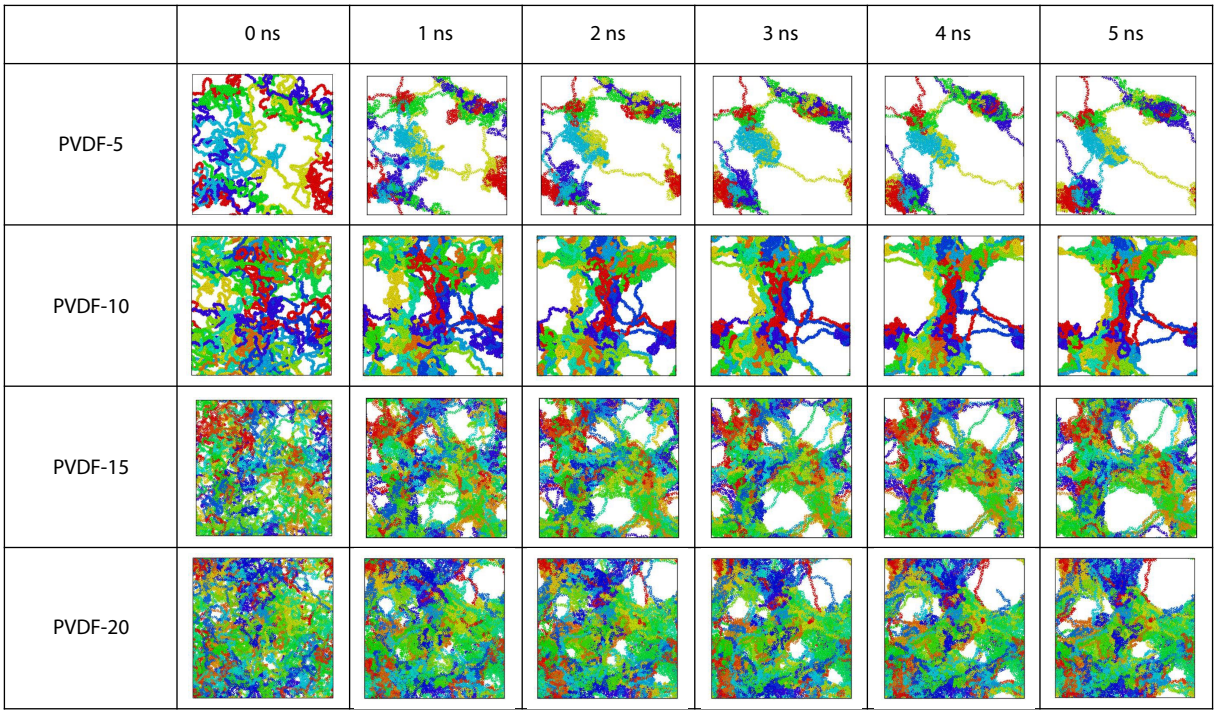


Fig. 7 Snapshots of the NIPS process at 298 K for systems with different concentrations of PVDF molecules having a polymerization degree of 1000.

https://doi.org/10.1007/s10118-026-3758-7

lar chains and the water molecules, as shown in Fig. 8(a). The interaction energies for PVDF-5, PVDF-10, PVDF-15, and PVDF-20 were all positive, thermodynamically confirming the repulsive interactions between PVDF and water molecules. In terms of the magnitude, $E_{PVDF-20} > E_{PVDF-15} > E_{PVDF-10} > E_{PVDF-5}$. This indicates that a higher initial PVDF content leads to greater interaction energy with the water phase, thereby enhancing the driving force for phase separation. Furthermore, the interaction energy curves for all the systems exhibited an evolutionary pattern characterized by a rapid initial decline followed by stabilization. This reflects the kinetic evolution of phase separation: initially, PVDF chains rapidly aggregate and contract to avoid the unfavorable aqueous environment, leading to the swift formation and sharpening of the interphase boundary (manifested as a steep drop in repulsive energy). Subsequently, the dominant phase region forms and reaches dynamic equilibrium, moderating the interface changes and causing the interaction energy to stabilize. The solubility parameters of PVDF in water at 0 and 5 ns were calculated, and their variations are shown in Fig. 8(b). The solubility parameter at 5 ns was lower than that at 0 ns, which revealed the structural evolution of the solution system from homogeneity to phase separation.

NIPS is a dynamic process involving continuous molecular motion. Fig. 9 illustrates how the PVDF molecular chain concentration affects mobility during NIPS. The MSD curves for systems with different PVDF concentrations at 298 K are shown in Fig. 9(a). The MSD of the PVDF molecular chains initially increased rapidly and then increased gradually over time. The high initial interaction energy between the PVDF and water molecules creates significant repulsive forces between them. The strong driving force for phase separation results in high initial mobility of the molecular chains. As the interaction force decreased during the middle and late stages of phase separation, the mobility of the molecular chains also diminished. Additionally, an inverse relationship was observed between increasing PVDF concentration and decreasing MSD curves. This indicates that higher PVDF concentrations reduce the molecular chain mobility during the NIPS process. This phenomenon arises from entanglement effects (Reputation theory):[50–53] adding large quantities of PVDF chains to the system intensifies chain entanglement. Increased entanglement enhances friction, thereby impeding the molecular chain motion.

The diffusion coefficient was calculated from the MSD curve shown in Fig. 9(b). At 298 K, the reduced concentration of PVDF molecular chains resulted in a higher diffusion coefficient for the chains. Similarly, the atomic displacement cloud diagram revealed more vigorous motion of the PVDF molecular chains in the low-concentration system. The diffusion coefficient of the PVDF-5 system was significantly higher than that of the PVDF-20 system, indicating that low-concentration PVDF chains exhibited greater mobility during the NIPS process. This is attributed to the following: in low-concentra-

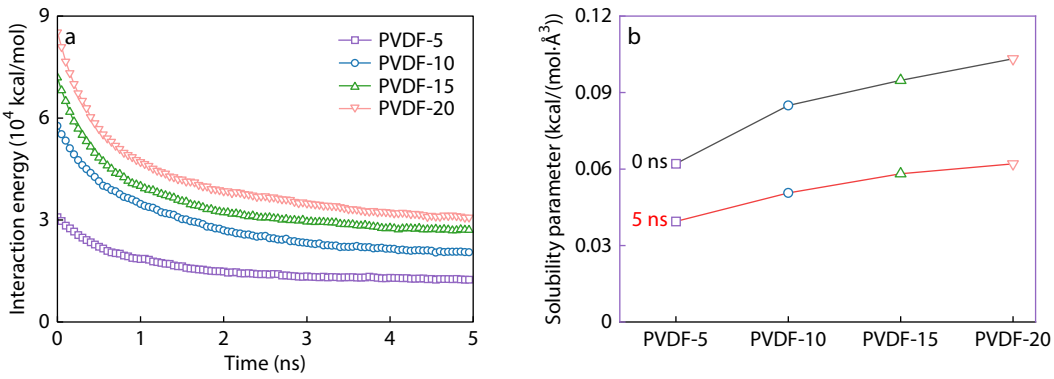


Fig. 8 At 298 K, (a) interaction energy-time curves and (b) comparison of solubility parameter changes before and after phase separation for PVDF systems at different concentrations during the NIPS process.

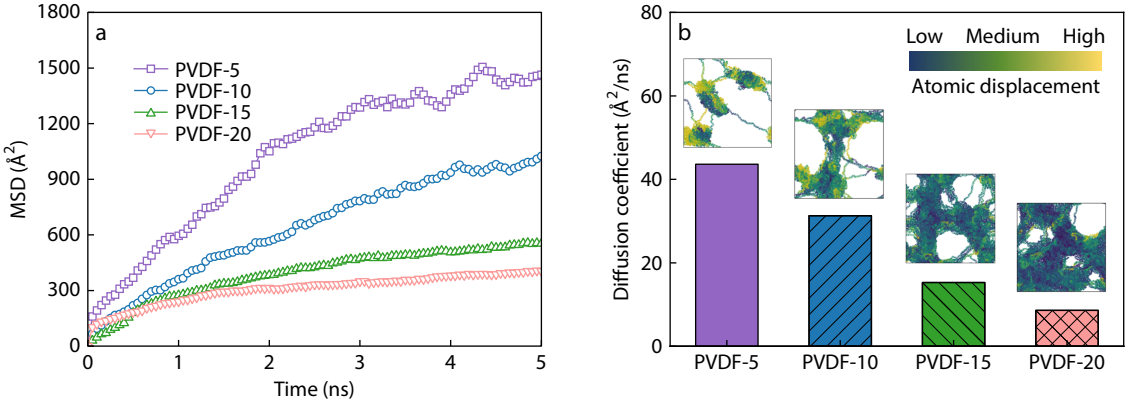


Fig. 9 At 298 K, (a) MSD-time curves and (b) diffusion coefficients and atomic displacement contour plots for PVDF systems at different concentrations during the NIPS process.

https://doi.org/10.1007/s10118-026-3758-7

tion systems, the initial entanglement level of the chains is low. To form a polymer-rich phase, the PVDF chains require long-range diffusion, which results in a higher apparent diffusion coefficient. Conversely, in high-concentration systems, the chains are densely packed and severely entangled. Strong topological constraints significantly limit segment motion, thereby diminishing their diffusion capacity. This concentration-dependent difference in the molecular chain diffusion capability is the key kinetic factor, ultimately leading to the formation of distinct porous morphologies.

During NIPS, the PVDF molecular chains underwent a gradual transition from uniform dispersion to concentrated enrichment. The entire NIPS process was visually tracked using a fluorine atom density cloud map (Fig. 10). In the initial state, the PVDF molecular chains were uniformly dispersed in the nonsolvent. When NIPS occurs at 5 ns, the system undergoes a dramatic phase reconstruction: the polymer precipitates from the nonsolvent, ultimately forming a two-phase structure that is significantly different from the initial state. The morphology of the final-state structure exhibited a significant concentration dependence. At low concentrations (PVDF-5), molecular chains aggregated into discrete island-like structures connected only by isolated single chains. When concentration increases to PVDF-10, the bridging transitions from "line" to "surface," with sheet-like structures emerging to link aggregates, initially forming a microporous structure filled with water molecules. By further increasing the concentration of PVDF-15, the system self-assembled into regular strip-like structures with uniform width, constructing channels with a consistent wall thickness. At the highest concentration (PVDF-20), the strip-like structures fused into an unevenly thick structure, ultimately resulting in pores with inconsistent wall thicknesses. The aforementioned morphological evolution clearly demonstrates that the initial PVDF concentration is the key factor regulating the final microstructure of the phase separation, which directly determines the pore morphology and wall thickness.

The final pore structure of the NIPS directly determines the performance of the separation membrane. The effects of different PVDF concentrations on pore volume evolution and final structure are shown in Fig. 11. Simulation results indicate that PVDF concentration significantly influences pore volume evolution and final structure: in the low-concentration system (PVDF-5), phase separation occurs rapidly, with pore volume stabilizing within 2 ns; whereas in the high-concentration system (PVDF-20), the phase separation process is significantly delayed, with pore volume stabilizing after 4 ns. This phenomenon aligns with the previously mentioned conclusions regarding the chain entanglement density and diffusion coefficient. Severe chain entanglement within high-concentration systems restricts molecular chain mobility, thereby delaying the pore evolution process from "pore nucleation" and "pore coalescence" to "through-pore expansion," ultimately slowing the rate of pore volume growth. Furthermore, the PVDF concentration determines the final pore volume. As the phase separation approaches equilibrium, the final pore volumes follow the pattern $V_{\text{PVDF-5}} > V_{\text{PVDF-10}} > V_{\text{PVDF-15}} > V_{\text{PVDF-20}}$. This indicates that higher polymer concentrations inhibit pore expansion, resulting in smaller and denser final pore structures. Using the initial pore volume of the PVDF-5 system as a reference (100%), the pore volume of the PVDF-20 system at 5 ns is 50.29% of that of the former. This finding aligns with the conclusions reported in literature.[54] A comparison of Figs.11(b)–11(e) also reveals the same phenomenon.

During the NIPS process, PVDF molecular chains aggregate to form a membrane skeleton, whereas the regions occupied by water molecules develop a pore structure after drying. To study the pore structure characteristics quantitatively, the system was divided into PVDF and water phases. Fig.12 shows the area comparison between the PVDF and water phases after phase separation in systems with different concentrations. The phase distribution comparison clearly reveals that the low-concentration systems (PVDF-5 and PVDF-10) tend to form fewer but larger pores, whereas the high-concentration systems (PVDF-15 and PVDF-20) produce nu-

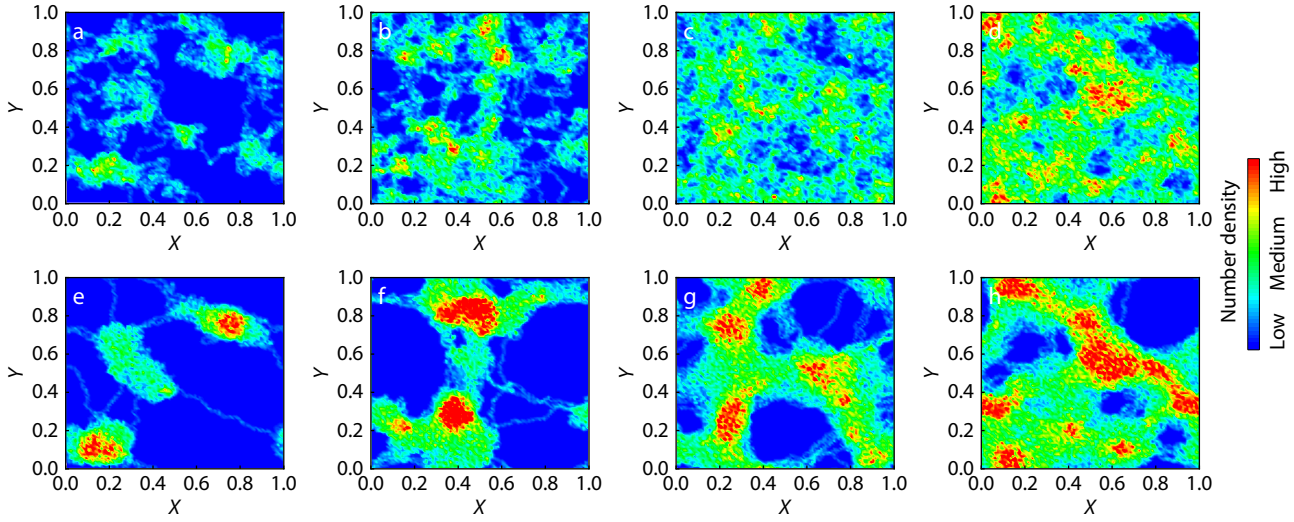


Fig. 10 Fluorine atom density contour plots of the initial state for PVDF systems at different concentrations at 298 K: (a) PVDF-5, (b) PVDF-10, (c) PVDF-15 and (d) PVDF-20. Fluorine atom number density contour plots at 5 ns after the onset of NIPS behavior: (e) PVDF-5, (f) PVDF-10, (g) PVDF-15 and (h) PVDF-20.

https://doi.org/10.1007/s10118-026-3758-7

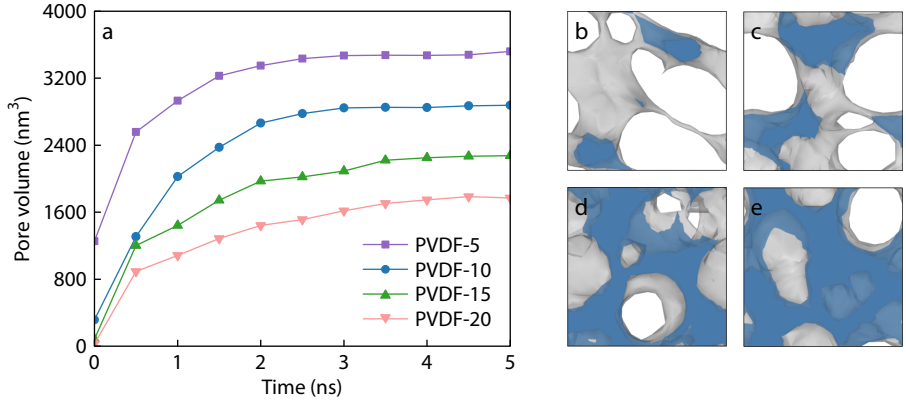


Fig. 11 (a) Pore volume evolution curves of PVDF systems at different concentrations during the NIPS process at 298 K. Snapshots of pore morphology formed by NIPS at 5 ns: (b) PVDF-5, (c) PVDF-10, (d) PVDF-15 and (e) PVDF-20.

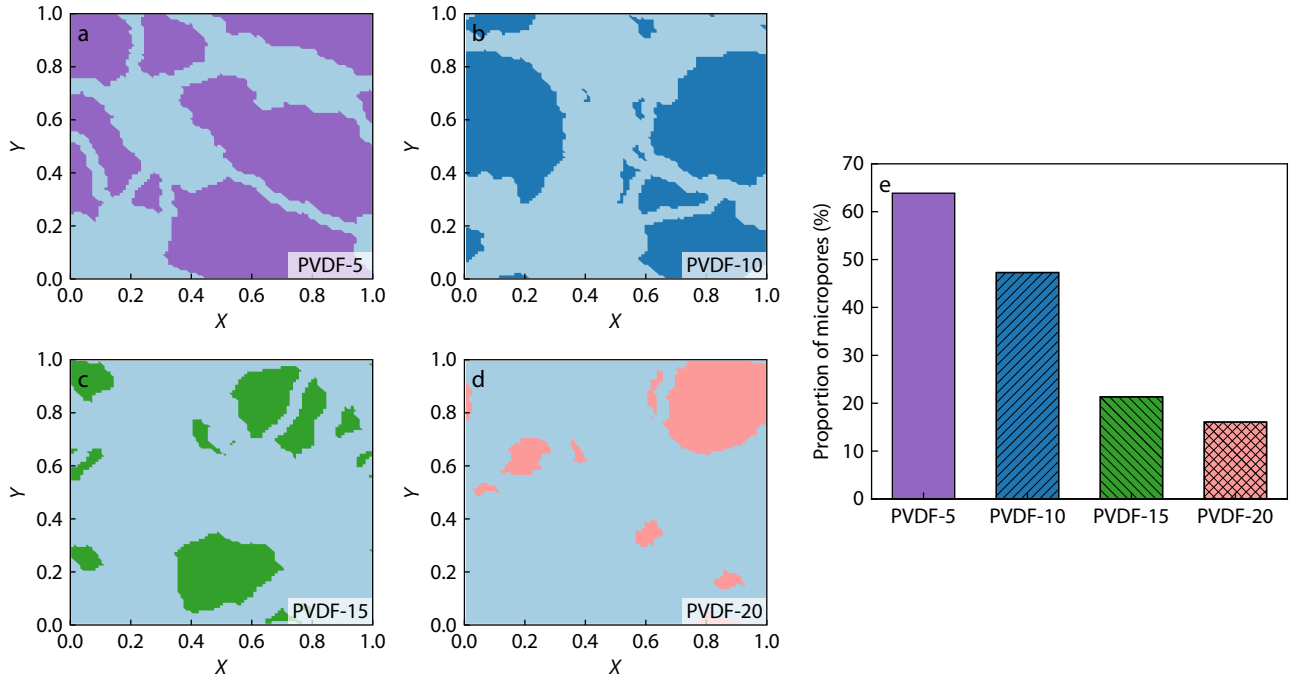


Fig. 12 At 298 K, area comparison of the water phase and PVDF phase 5 ns after NIPS behavior onset in systems with different concentrations: (a) PVDF-5, (b) PVDF-10, (c) PVDF-15 and (d) PVDF-20. (e) Column chart showing pore area fraction formed 5 ns after NIPS behavior onset.

merous smaller pores. Quantifying the pore area data from the figure above yields the proportion of pore area after phase separation, as shown in Fig. 12(e). The order of pore area proportions was PVDF-5 > PVDF-10 > PVDF-15 > PVDF-20. This phenomenon stems from the decisive influence of the initial polymer concentration on the phase separation thermodynamics; higher PVDF concentrations result in a smaller volume fraction of the polymer-poor phase formed after phase separation. Higher PVDF concentrations resulted in a smaller volume fraction of polymer-depleted phase formed after phase separation. This inevitably reduced the total volume of the pore phase derived from the polymer-poor phase and the corresponding pore volume, thereby forming a denser porous structure with finer pore sizes.

Temperature Dependence

To investigate the effect of temperature on the NIPS process, MD simulations were conducted for systems with identical concentrations at different temperatures. Fig. 13 shows visualizations of the NIPS process in a system containing 10 PVDF molecular chains at temperatures of 273, 298, and 333 K (water molecules hidden). At 273 K, numerous uniformly sized pores appear within 1 ns and subsequently coalesce slowly into larger pores. After 3 ns of NIPS, the number of pores stabilized, whereas the pore volume began to increase. At 5 ns, phase separation of the system at 273 K resulted in the formation of a stable structure. At 298 K, pores of various sizes appeared as early as 1 ns. As phase separation progressed, the large pores in the 298 K system gradually expanded, while the small pores gradually disappeared. After 3 ns of phase separation, the pore structure remained largely unchanged, indicating that the phase separation process was complete, and a stable structure was formed. At 333 K, large pores also appeared within 1 ns, but equilibrium was reached more rapidly, with phase separation concluding at

https://doi.org/10.1007/s10118-026-3758-7

2 ns, and pore shapes no longer changing. Overall, temperature had little effect on the pore structure formed after NIPS but significantly influenced the speed of the NIPS process.

The effect of temperature on the NIPS process was determined by analyzing the magnitude of the interaction energies in the same model at different temperatures. Fig. 14(a) shows the interaction energy variation curves for the NIPS process at 273, 298, and 333 K in a system containing 10 PVDF molecular chains with a polymerization degree of 1000. The interaction energy curve indicates that the influence of the temperature-dependent interaction energy is negligible in the initial state, but as NIPS behavior occurs, the interaction energy decreases. However, the rate of decrease was the fastest at 333 K, followed by 298 K, with the slowest decrease observed at 273 K. During the late phase of phase separation, the interaction energy stabilized and ceased to decrease, with values ordered as $E_{273\ K} > E_{298\ K} > E_{333\ K}$. This indicates that the temperature influences the NIPS process, with higher temperatures increasing the phase-separation driving force. Similarly, Fig. 14(b) shows the solubility parameters of PVDF in water, calculated using the interaction energy. The solubility parameter at 5 ns was lower than that at 0 ns, indicating the precipitation of PVDF during the phase separation. The difference in solubility parameter values at different temperatures suggests that temperature has a smaller effect on the interaction energy than the polymer concentration.

The effect of temperature on the phase separation rate was determined by studying the mobility of the PVDF molecular chains in the systems at different temperatures. Fig. 15(a) shows the MSD curves of the PVDF molecular chains during the NIPS process at 273, 298, and 333 K. The MSD curves exhibit similar trends, but grow at different rates. The MSD curve for the PVDF chains at 333 K increased most rapidly, followed by that at 298 K, while the curve at 273 K exhibited the slowest growth rate. This phenomenon arises because the motion of the PVDF chains within the system is influenced by molecular thermal motion.[20,55] All the microscopic particles were constantly engaged in random motion. The kinetic theory of gases serves as a bridge connecting the behavior of microscopic particles to that of macroscopic phenomena. Temperature influences the thermal motion of microscopic particles; as the temperature increases, the thermal motion be-

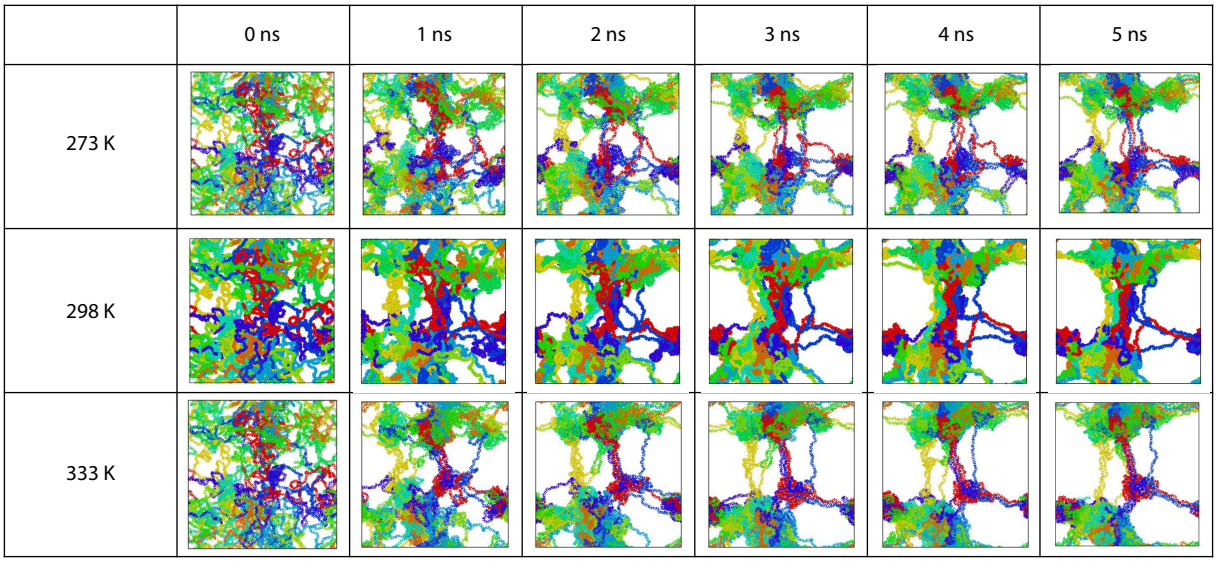


Fig. 13 Snapshots of the NIPS process at different temperatures when the system contains 10 PVDF molecular chains with a polymerization degree of 1000.

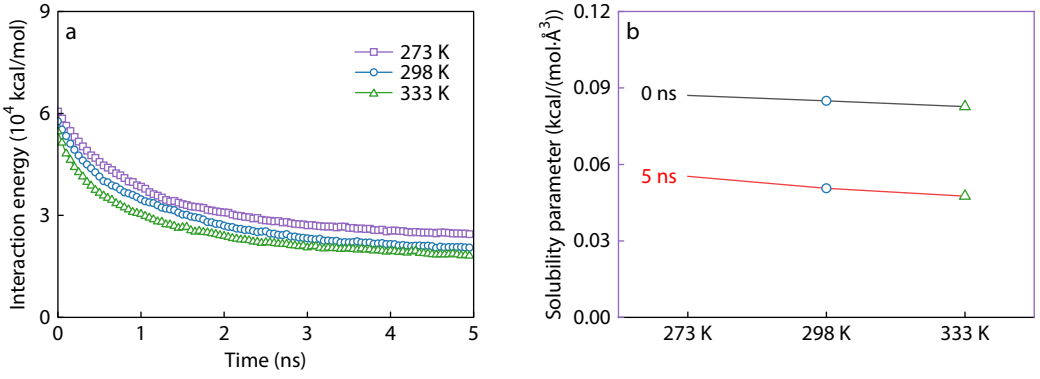


Fig. 14 When the system contains 10 PVDF molecular chains with a polymerization degree of 1000, (a) interaction energy-time curves and (b) comparison of solubility parameter changes before and after phase separation during the NIPS process at different temperatures.

https://doi.org/10.1007/s10118-026-3758-7

comes more intense. This further leads to the macroscopic phenomena of different phase separation rates. The fundamental reason lies in the fact that the increased temperature enhances the free volume of microscopic particles, resulting in the macroscopic phenomenon of enhanced mobility within the molecular chains.

The thermal motion of polymers includes micro-Brownian motion performed by independently moving segments, and macro-Brownian motion performed by the entire polymer chain.[56,57] The diffusion coefficients of the PVDF chains during NIPS at 273, 298, and 333 K were calculated from the MSD curves, as shown in Fig. 15(b). At a fixed concentration of PVDF chains in the system, the diffusion coefficient increased significantly with increasing temperature. Similarly, the atomic displacement map revealed that higher temperatures resulted in a greater displacement of the PVDF fragments. The initial model of the system undergoing NIPS at 273, 298, and 333 K is identical, meaning that the entanglement states of the molecular chains are consistent. Constrained by entanglement, the macro-Brownian motion of the molecular chains was suppressed during the NIPS process at different temperatures. However, micro-Brownian motion remains active. This motion alters the conformation through the internal rotation of C—C bonds along the main chain, enabling short-range movements such as hopping and twisting within local chain segments. The higher the system temperature, the more pronounced is the micro-Brownian motion of the PVDF segments. This is the primary reason for the increased diffusion coefficient of PVDF molecular chains at elevated temperatures.

Temperature is a key parameter that influences the NIPS process and the final structure. To investigate its role, we statistically analyzed the elemental distribution during phase separation and plotted the fluorine atom number density contour plots at 273, 298, and 333 K, as shown in Fig. 16. Before phase separation occurs, the fluorine atoms are uniformly dispersed throughout the system. However, after 5 ns of phase separation, the PVDF molecular chains underwent significant enrichment, forming a stable two-phase structure in the final state. Although the macroscopic morphologies of the phase-separated structures formed at different temperatures are similar, the areas of the highly enriched fluorine regions (red areas) exhibit significant differences. The surface area increased with increasing temperature in the following order: 273 K < 298 K < 333 K. This indicates that at the same phase separation time, elevated temperatures promote the aggregation of the PVDF molecular chains. This ultimately leads to a higher degree of PVDF enrichment. This phenomenon is primarily attributed to the temperature regulation of molecular chain mobility: elevated temperatures provide the system with greater thermal kinetic energy, significantly accelerating the motion and migration rate of PVDF molecular chains. This enables the molecular chains to move and aggregate more rapidly under phase-separation driving forces, thereby achieving a higher degree of enrichment within the same timeframe.

The influence of temperature on NIPS behavior can be further revealed through the evolution of the pore volume and differences in the final-state structures. Fig. 17 displays the pore volume variation curves during the NIPS process at different temperatures and the corresponding final state structural simulation snapshots. The pore volume evolution curves

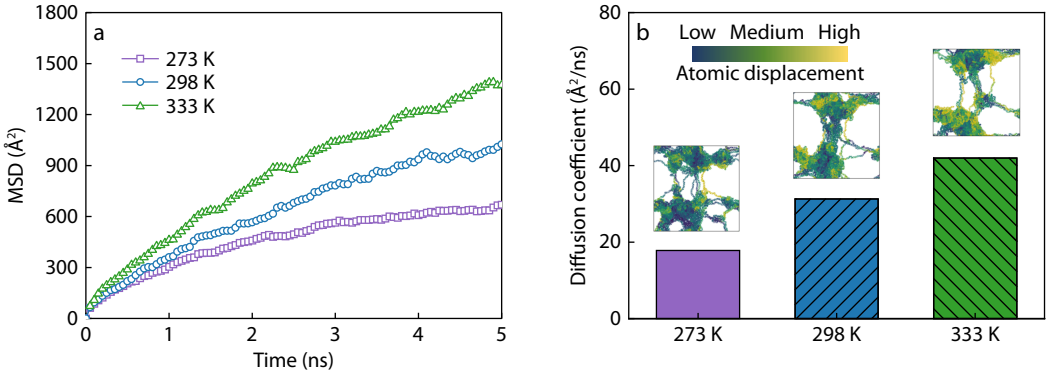


Fig. 15 (a) MSD-time curves and (b) diffusion coefficients and atomic displacement contour plots of the NIPS process at different temperatures for the system contains 10 PVDF molecular chains with a polymerization degree of 1000.

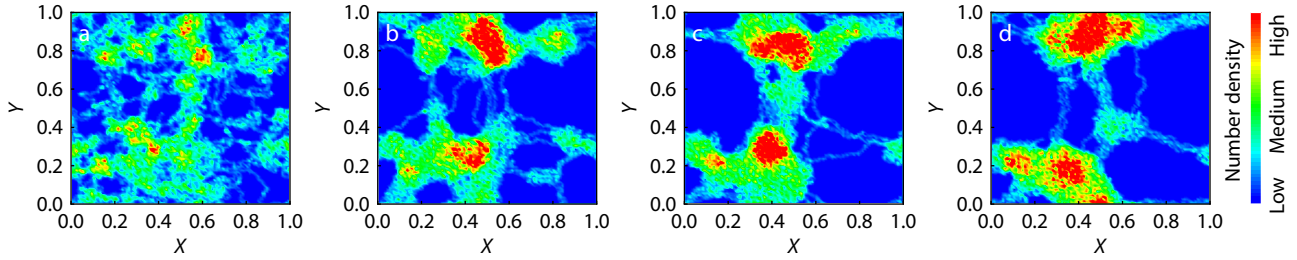


Fig. 16 Fluorine atom density contour plots of (a) the initial model containing 10 PVDF molecular chains with a polymerization degree of 1000. Fluorine atom density contour plots at 5 ns after NIPS onset: (b) at 273 K, (c) at 298 K and (d) at 333 K.

https://doi.org/10.1007/s10118-026-3758-7

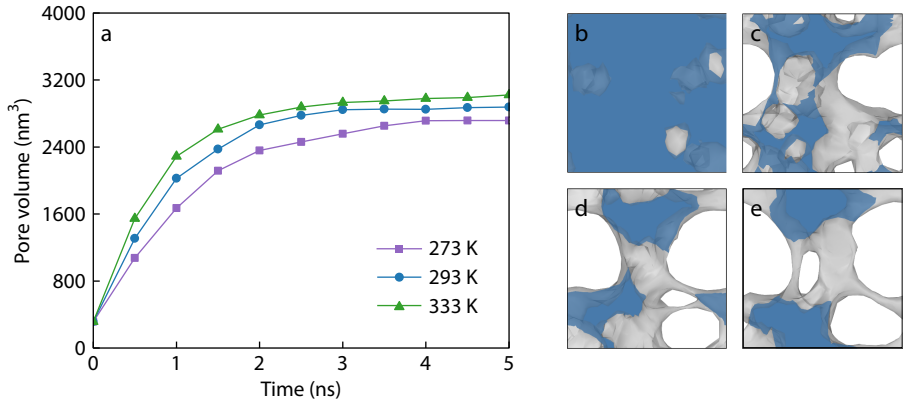


Fig. 17 (a) Pore volume-time curves of the NIPS process at different temperatures for a system contains 10 PVDF molecular chains with a polymerization degree of 1000. Snapshots of pore morphology (b) at the initial structure and 5 ns after NIPS occurrence at system temperatures of (c) 273 K, (d) 298 K and (e) 333 K.

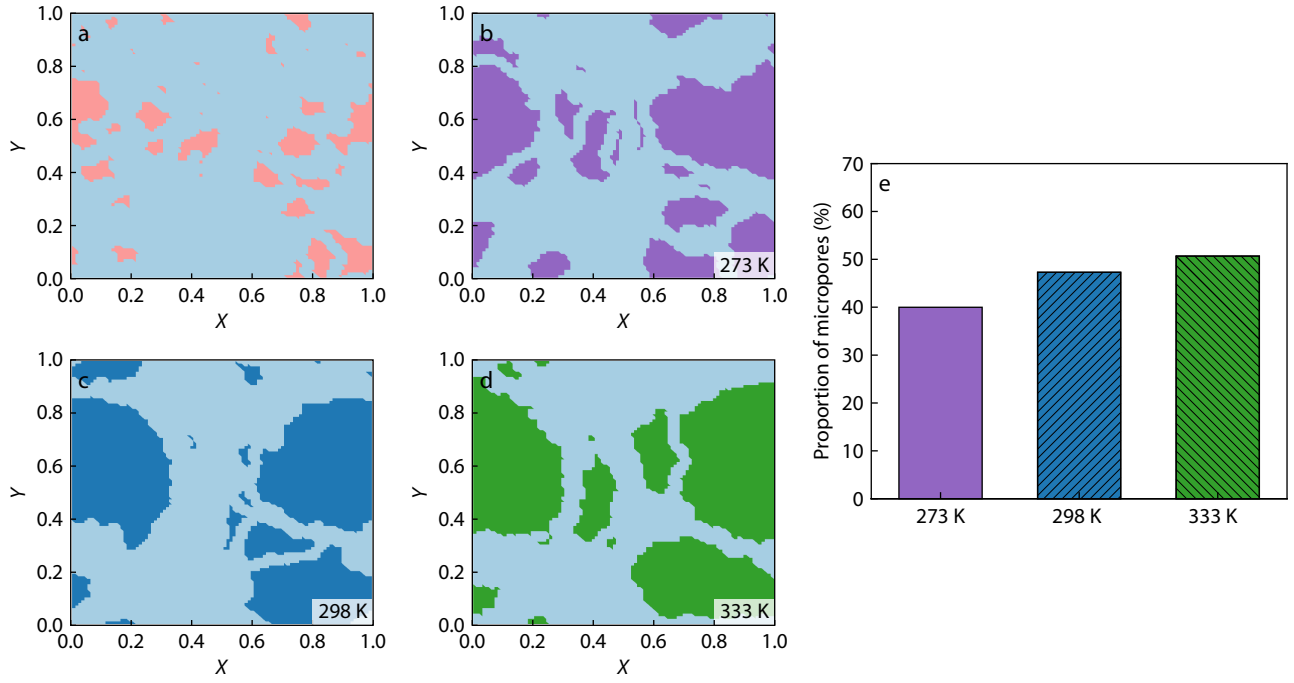


Fig. 18 (a) The area ratio between the H_2O phase and the PVDF phase in the initial model containing 10 PVDF molecular chains with a polymerization degree of 1000. The area ratio between the H_2O phase and the PVDF phase after 5 ns of NIPS behavior is presented at system temperatures of (b) 273 K, (c) 298 K and (d) 333 K, along with (e) the pore area fraction.

demonstrate that the temperature significantly affects both the formation kinetics of the pore structures and the final pore size. At 333 K, the pore volume increased rapidly and stabilized after 2 ns, with the final pore volume significantly higher than that of the other two groups. When the temperature was lowered to 298 K, the rate of pore volume growth slowed down, stabilizing after only 3 ns, and the final pore volume was smaller than that of the 333 K system. At a low temperature of 273 K, the pore volume growth was the slowest, and the final pore size was the smallest among the three. The aforementioned phenomenon is closely related to the regulatory effect of temperature on molecular chain mobility; elevated temperatures significantly enhance the migration rate of PVDF molecular chains, thereby accelerating the phase separation process. The higher phase separation rate promotes faster growth of the pore volume, enabling the system to reach thermodynamic equilibrium more rapidly under high-temperature conditions and form a more developed pore structure. The final pore volume significantly increased with increasing temperature. Specifically, from 273 K to 333 K, the 60 K temperature increase led to an approximately 11.23% greater pore volume, further confirming the positive promotion of pore evolution by temperature during NIPS. The temperature-dependent pore growth is attributed to pore coalescence and expansion driven by diffusion. The increased molecular mobility (the temperature dependence of the diffusion coefficient is shown in Fig. 15). accelerates the frequency of collisions and mergers between adjacent pores, thereby forming larger interconnected pores within the same timeframe. Consequently, increasing the temperature accel-

https://doi.org/10.1007/s10118-026-3758-7

erated the rate of pore expansion, further increasing the pore size.

NIPS behavior separates the homogeneous system into polymer-rich and polymer-poor phases. The polymer-poor phase forms pores after drying. To investigate the characteristics of the porous structures obtained through NIPS, the phase-separated model was divided into PVDF and H_2O phases. Different colors were used to distinguish the PVDF and H_2O phases, as shown in Fig. 18. At 273 K, the system formed numerous small pores after the phase separation. When the temperature was increased to 298 K, the pores formed after phase separation increased in size, while the number of small pores decreased. At 333 K, micropores coalesced into macropores. Quantifying the pore area yields the pore distribution shown in Fig. 18(e). The proportion of micropores decreased in the order 333 K > 298 K > 273 K. This indicates that as the temperature of the system increased, the degree of phase separation also increased. The temperature increase intensifies the molecular thermal motion, accelerating the migration speed of the molecular chains, thereby enhancing the phase separation of the system.

CONCLUSIONS

This study employed an all-atom MD simulation to reveal the microscopic mechanism of the NIPS process at the atomic scale. This study delves into two variables: polymer concentration and system temperature. The study delves into the interaction energy, diffusion coefficient, and pore volume data during phase separation, and further analyzes their impact on the NIPS process. The strong interaction between the water molecules and fluorine atoms on the PVDF molecular chains thermodynamically confirms the repulsive force between the PVDF and water molecules. This constitutes the fundamental driver of phase separation. Furthermore, comparisons were made between laboratory-synthesized microporous polymer membranes and the simulated pore structures. The MD simulations successfully reproduced the key topological parameters observed experimentally, such as the symmetric pore structure and connectivity, capturing the equilibrium structure under experimental conditions. This comparative analysis not only demonstrates the reliability of the simulations, but also provides a foundation for subsequent predictive studies based on this methodology.

MD simulations indicated that polymer concentration influenced both the rate and pore morphology of the NIPS process. Higher polymer concentrations within the same volume lead to more severe entanglement between the polymer chains, consequently reducing the phase-separation rate. Furthermore, polymer concentration determines the volume fraction occupied by the polymer-rich phase formed during phase separation, resulting in distinct pore morphologies after separation. The pore volumes after phase separation followed the order $V_{PVDF\text{-}5} > V_{PVDF\text{-}10} > V_{PVDF\text{-}15} > V_{PVDF\text{-}20}$. When the system temperature varied while the polymer concentration remained constant, the effect of temperature on the phase separation rate became more pronounced. Under high-temperature conditions, the thermal motion of the molecular chains intensifies, thereby accelerating phase separation. At system temperatures of 273, 298 and 333 K, the diffusion coefficients of PVDF molecular chains are 17.81, 31.31 and 41.95 Å^2/ns, respectively. The pore volumes during phase separation were $V_{333\,K} > V_{298\,K} > V_{273\,K}$. MD simulations enabled the visualization of dynamic processes, capturing the entire structural evolution pathway. They provided a precise analysis of the intermolecular interactions and revealed intermediate states that are difficult to observe through conventional experiments. Furthermore, these simulations facilitate efficient screening by elucidating polymer-non-solvent interaction mechanisms and enabling phase separation simulations under highly toxic or extreme conditions, thereby providing guidance for the experiment.

Conflict of Interests

The authors declare no interest conflict.

Electronic Supplementary Information

Electronic supplementary information (ESI) is available free of charge in the online version of this article at http://doi.org/10.1007/s10118-026-3758-7.

Data Availability Statement

The data supporting the findings of this study are available from the corresponding author upon reasonable request.

ACKNOWLEDGMENTS

This work was financially supported by the National Natural Science Foundation of China (No. 51503078), Science Technology-Based Small and Medium-Sized Enterprises Innovation Capacity Enhancement Project of Shandong Province (No. 2023TSGC0589), and Natural Science Foundation of Shandong Province (No. ZR2013EMQ002).

REFERENCES

1 Costa, C. M.; Cardoso, V. F.; Martins, P.; Correia, D. M.; Gonçalves, R.; Costa, P.; Correia, V.; Ribeiro, C.; Fernandes, M. M.; Martins, P. M.; Lanceros-Méndez, S. Smart and multifunctional materials based on electroactive poly(vinylidene fluoride): recent advances and opportunities in sensors, actuators, energy, environmental, and biomedical applications. *Chem. Rev.* **2023**, *123*, 11392–11487.

2 Saeed, A. M.; Saied, M. A.; Szymoniak, P.; Altmann, K.; Schönhals, A.; Fahmy, A. High performance novel polyelectrolyte membrane consisting of polyvinyl alcohol-phenylsilanol-polypyrrole. *Appl. Surf. Sci.* **2026**, *731*, 166495.

3 Wang, Z.; Liu, J.; Yi, K.; Chen, P.; Zhu, Y.; Tian, D.; Chu, B. Shape memory effect and light-induced deformation in schiff base molecular crystals/PVDF ferroelectric polymer composites. *Chem. Eng. J.* **2023**, *455*, 140693.

4 Wang, H.; Zhang, W.; Jia, S.; Wang, C.; Feng, Y. Construction of antifouling and renewable nanofiltration membranes through surface self-assembly for dye/salt separation. *Appl. Surf. Sci.* **2026**, *723*, 165611.

5 Zhang, X.; Zhao, Y.; Wang, M. pH-Responsive zwitterionic membranes: fabrication and mechanism of UiO-66-

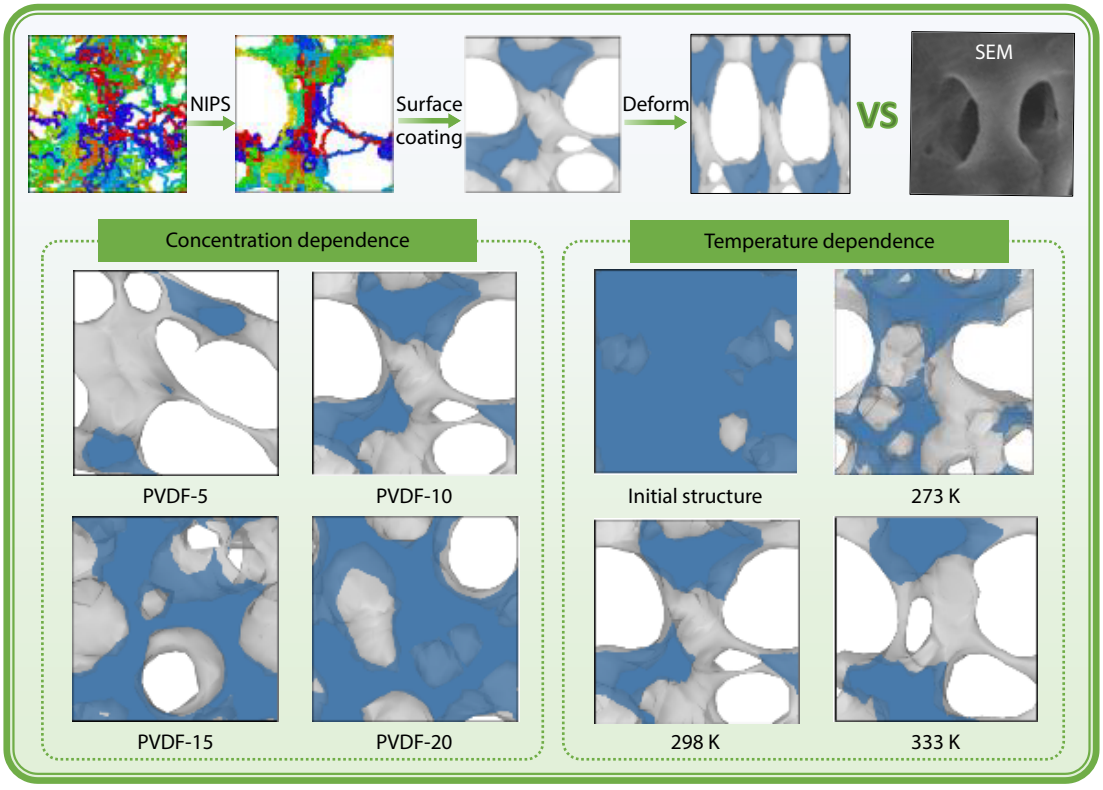
Graphical Abstract

Microscopic Insights into the Mechanism of Microporous Polymer Membrane Preparation by Non-solvent Induced Phase Separation: a Molecular Dynamics Simulation Study

Ji-Tao Liu, Yue-Ying Sun, Xin-Ran Dai, Zhi-Hao Zong, Shuai Li, Yan-Chen Li, and Chun-Sheng Li

University of Jinan

This study has achieved atomic-level simulation of the NIPS process and provides theoretical guidance for optimizing the manufacturing process parameters of polymer microporous membranes.



Chinese J. Polym. Sci. 2026 *https://doi.org/10.1007/s10118-026-3758-7*

PYDC/sulfonated polysulfone hybrid ultrafiltration membranes. *Appl. Surf. Sci*. **2026**, *720*, 165344.

6 Tang, Y.; Lin, Y.; Ma, W.; Wang, X. A review on microporous polyvinylidene fluoride membranes fabricated *via* thermally induced phase separation for MF/UF application. *J. Membr. Sci.* **2021**, *639*, 119759.

7 Yu, H.; Shangguan, S.; Yang, H.; Rong, H.; Qu, F. Chemical cleaning and membrane aging of poly(vinylidene fluoride) (PVDF) membranes fabricated *via* non-solvent induced phase separation (NIPS) and thermally induced phase separation (TIPS). *Sep. Purif. Technol.* **2023**, *313*, 123488.

8 Zarghami, S.; Mohammadi, T.; Sadrzadeh, M.; Van Der Bruggen, B. Superhydrophilic and underwater superoleophobic membranes—a review of synthesis methods. *Prog. Polym. Sci.* **2019**, *98*, 101166.

9 Yang, C.; Zhu, G.; Yi, Z.; Zhou, Y.; Gao, C. Critical Contributions of additives on the fabrication of asymmetric isoporous membranes from block copolymers: a review. *Chem. Eng. J.* **2021**, *424*, 128912.

10 Mahajan, S.; Li, Y. Toward molecular simulation guided design of next-generation membranes: challenges and opportunities. *Langmuir* **2025**, *41*, 12388−12402.

11 Cervellere, M. R.; Qian, X.; Ford, D. M.; Carbrello, C.; Giglia, S.; Millett, P. C. Phase-field modeling of non-solvent induced phase separation (NIPS) for PES/NMP/Water with comparison to experiments. *J. Membr. Sci.* **2021**, *619*, 118779.

12 Blagojevic, N.; Müller, M. Simulation of membrane fabrication *via* solvent evaporation and nonsolvent-induced phase separation. *ACS Appl. Mater. Interfaces* **2023**, *15*, 57913−57927.

13 Cervellere, M. R.; Tang, Y.; Qian, X.; Ford, D. M.; Millett, P. C. Mesoscopic simulations of thermally-induced phase separation in PVDF/DPC solutions. *J. Membr. Sci.* **2019**, *577*, 266−273.

14 Liu, W.; Bai, H.; Zhang, Q.; Zhang, Z.; Li, W.; Wang, H.; Lu, S.; Xiang, Y. Microscopic insight into phase separation of poly (arylene piperidine)s-based high-temperature proton exchange membrane: a molecular simulation study. *J. Membr. Sci.* **2024**, *698*, 122616.
15 Theodorakopoulos, G. V.; Karousos, D. S.; Favvas, E. P.; Gotzias, A. D. Formation of polyimide membranes *via* non-solvent induced phase separation: insight from molecular dynamics simulations. *ChemPlusChem* **2024**, *89*, e202300766.
16 Plimpton, S. Fast parallel algorithms for short- range molecular dynamics. *J. Comput. Phys.* **1995**, *117*, 1–19.
17 Sun, H. Ab Initio calculations and force field development for computer simulation of polysilanes. *Macromolecules* **1995**, *28*, 701–712.
18 Sun, H. Force field for computation of conformational energies, structures, and vibrational frequencies of aromatic polyesters. *J. Comput. Chem.* **1994**, *15*, 752–768.
19 Sun, H.; Mumby, S. J.; Maple, J. R.; Hagler, A. T. An ab initio CFF93 all-atom force field for polycarbonates. *J. Am. Chem. Soc.* **1994**, *116*, 2978–2987.
20 Yang, J.; Yao, X.; Meng, Z. Investigation of molecular mechanisms of polyvinylidene fluoride under the effects of temperature, electric poling, and mechanical stretching using molecular dynamics simulations. *Polymer* **2022**, *245*, 124691.
21 Sun, Y. Y.; Dai, X. R.; Xie, Z. B.; Li, S.; Tang, X. L.; Liu, J. T. Effect of shear deformation and temperature history on crystal transformation of polyvinylidene fluoride/silica composites: a molecular dynamics study. *Polym. Compos*. **2025**, pc.70197.
22 Sun, Y.-Y.; Tang, X.-L.; Dai, X.-R.; Zheng, L.; Liu, J.-T. Molecular dynamics study on the shear deformation process and crystal transformation of polyvinylidene fluoride. *Mater. Today Commun.* **2024**, *41*, 111017.
23 Li, Y.; Li, G.; Lyu, W. Microstructure and mechanical property analysis of HTPB adhesive under thermal aging based on molecular dynamic simulations. *Mater. Today Commun.* **2024**, *38*, 107919.
24 Smith, P. E.; Gunsteren, F. The viscosity of spc and spc/e water at 277 and 300 K. *Chem. Phys. Lett.* **1993**, *215*, 315–318.
25 Guevara-Carrion, G.; Vrabec, J.; Hasse, H. Prediction of self-diffusion coefficient and shear viscosity of water and its binary mixtures with methanol and ethanol by molecular simulation. *J. Chem. Phys.* **2011**, *134*, 074508.
26 Sun, H. COMPASS: An ab initio force-field optimized for condensed-phase applications overview with details on alkane and benzene compounds. *J. Phys. Chem. B* **1998**, *102*, 7338–7364.
27 Rezaei, R.; Shariati, M.; Tavakoli-Anbaran, H.; Deng, C. Mechanical characteristics of cnt-reinforced metallic glass nanocomposites by molecular dynamics simulations. *Comput. Mater. Sci.* **2016**, *119*, 19–26.
28 Ain, Q. U.; Wani, M. F.; Sehgal, R.; Singh, M. K. Mechanical and viscoelastic characterization of Al_2O_3 based polymer nanocomposites: an experimental and molecular dynamics simulation approach. *Comput. Mater. Sci.* **2024**, *239*, 112955.
29 Stukowski, A. Visualization and analysis of atomistic simulation data with OVITO–the open visualization tool. *Model. Simul. Mater. Sci. Eng.* **2010**, *18*, 015012.
30 Li, C.; Strachan, A. Cohesive energy density and solubility parameter evolution during the curing of thermoset. *Polymer* **2018**, *135*, 162–170.
31 He, L.; Zhang, W.; Shi, P.; Liu, S.; Li, G.; Alexiadis, A.; Tao, M.; Van Den Bergh, W.; Del Barco Carrión, A. J.; Zhukouski, Y.; Mladenovic, G.; Rzek, L.; Valentin, J.; Kowalski, K. J.; Mohd Hasan, M. R. Phase separation behavior of eco-friendly warm mixed sbs modified asphalt: a molecular dynamics and phase field approach. *J. Clean. Prod.* **2025**, *501*, 145258.
32 Qian, D.; Michaels, T. C. T.; Knowles, T. P. J. Analytical solution to the flory–huggins model. *J. Phys. Chem. Lett.* **2022**, *13*, 7853–7860.
33 Antoine, S.; Geng, Z.; Zofchak, E. S.; Chwatko, M.; Fredrickson, G. H.; Ganesan, V.; Hawker, C. J.; Lynd, N. A.; Segalman, R. A. Flory-Huggins s interaction parameters in polyether-based polymers. *Macromolecules* **2021**, *54*, 6670–6677.
34 Liu, Y.; Zhang, J.; Li, J.; Zhao, Y.; Zhang, M. Impact of SiO_2 doping on the structure and oil–water separation properties of a pvdf membrane: insights from molecular dynamics simulation. *RSC Adv.* **2024**, *14*, 23910–23920.
35 Zhang, H.; Liu, W.; Xu, H.; Zhuo, Q.; Sun, X. Adsorption behavior of methyl laurate and dodecane on the sub-bituminous coal surface: molecular dynamics simulation and experimental study. *Minerals* **2019**, *9*, 30.
36 Huang, B.; Zhao, R.; Xu, H.; Deng, J.; Li, W.; Wang, J.; Yang, H.; Zhang, L. Adsorption of methylene blue on bituminous coal: adsorption mechanism and molecular simulation. *ACS Omega* **2019**, *4*, 14032–14039.
37 Xing, W.; Yan, Y.; Xu, L. Boosting the precise separation of specific molecules using molecularly imprinted membranes through the synergism of hierarchically structured porous and thin selective layers. *J. Membr. Sci.* **2025**, *731*, 124236.
38 He, X.; Dugas, M. P.; Hodul, J. N.; Boudouris, B. W.; Phillip, W. A. Porous block polymer composite membranes for uranium uptake. *Appl. Surf. Sci.* **2024**, *643*, 158650.
39 An, Y.; Li, F.; Wang, H.; Zhang, X.; Di, Y.; Wang, L.; Yan, Z.; Wang, W.; Lu, J.; Liu, M.; Fei, P. Preparation and properties of cellulose triacetate (CTA)-PVDF composite membrane with hydrophobic/hydrophilic properties for membrane distillation. *Appl. Surf. Sci.* **2025**, *684*, 161891.
40 Maghami, M.; Abdelrasoul, A. Pair interaction energy decomposition analysis (pieda) and experimental approaches for investigating water interactions with hydrophilic and hydrophobic membranes. *J. Mol. Graph. Model.* **2020**, *96*, 107540.
41 Biswas, B.; Singh, P. C. The role of fluorocarbon group in the hydrogen bond network, photophysical and solvation dynamics of fluorinated molecules. *J. Fluor. Chem.* **2020**, *235*, 109414.
42 Kitabata, M.; Taddese, T.; Okazaki, S. Molecular dynamics study on wettability of poly(vinylidene fluoride) crystalline and amorphous surfaces. *Langmuir* **2018**, *34*, 12214–12223.
43 Zhang, H.; Deng, S.; Zhang, J.; Wang, D.; Fan, H.; Xu, Y.; Zhao, F.; Chen, Q.; Wang, J. Design, characterization, and structure-function relationships of modified polyvinylidene fluoride membranes for water treatment. *J. Membr. Sci.* **2025**, *728*, 124120.
44 Leichtweis, J.; Vieira, Y.; Carissimi, E.; Ulbricht, M.; Fischer, L. Photocatalytic and persulfate-facilitated tetracycline degradation using nife2o4/carbon/polymer membranes: activity and stability during flow-through. *Appl. Surf. Sci.* **2024**, *669*, 160603.
45 Kulak, H.; Swings, W.; Cools, M.; Hannes, L.; Vankelecom, I. F. J. Developing silver-decorated polyimide asymmetric membranes using green solvents for olefin/paraffin gas separations. *J. Membr. Sci.* **2025**, *734*, 124404.
46 Liu, S.; Ge, M.; Meng, L.; Liu, X.; Fang, T. Mechanism analysis of CO_2 separation from pvdf-supported deep eutectic solvent:a molecular dynamics simulation study. *J. Mol. Liq.* **2024**, *403*, 124806.
47 Costa, C. M.; Kundu, M.; Cardoso, V. F.; Machado, A. V.; Silva, M. M.; Lanceros-Méndez, S. Silica/poly(vinylidene fluoride) porous composite membranes for lithium-ion battery separators. *J. Membr. Sci.* **2018**, *564*, 842–851.
48 Hampu, N.; Werber, J. R.; Chan, W. Y.; Feinberg, E. C.; Hillmyer, M. A. Next-generation ultrafiltration membranes enabled by block polymers. *ACS Nano* **2020**, *14*, 16446–16471.

49 Prihartini Aryanti, P. T.; Nugroho, F. A.; Lugito, G.; Khoiruddin, K. Tight ultrafiltration membranes: advancing separation technologies for water and wastewater treatment. *Sep. Purif. Technol.* **2025**, *367*, 132892.

50 Peng, F.; Cao, R.; Sun, H.; Liu, Z.; Zhang, Y.; Xu, T.; Li, L. Role of entanglement in polymer crystal growth and melting: molecular dynamics simulations. *Macromolecules* **2024**, *57*, 10487−10498.

51 Zou, L.; Zhang, W. Molecular dynamics simulations of the effects of entanglement on polymer crystal nucleation. *Macromolecules* **2022**, *55*, 4899−4906.

52 Wu, L. F.; Mao, L. F.; Wang, Z. Effective entanglement and constraint release in deformed polymer melts. *Macromolecules* **2024**, *57*, 3202−3211.

53 Korolkovas, A.; Gutfreund, P.; Wolff, M. Dynamical structure of entangled polymers simulated under shear flow. *J. Chem. Phys.* **2018**, *149*, 074901.

54 Cheng, P.; Liu, M.; Tian, G.; Tang, Q.; Xiang, J.; Zhang, L.; Tang, N. Study on vacuum membrane distillation performance of pp/poe blending membranes prepared *via* thermally induced phase separation using bidiluent. *Sep. Purif. Technol.* **2021**, *274*, 118475.

55 Volkov, V. V.; Fadeev, A. G.; Plate, N. A.; Amaya, N.; Murata, Y.; Takanara, A.; Kajiyama, T. Effect of thermal molecular motion on pervaporation behavior of comb-shaped polymers with fluorocarbon side groups. *Polym. Bull.* **1994**, *32*, 193−200.

56 Ito, K. Studies on straining of high polymer solids. *J. Polym. Sci.* **1958**, *27*, 419−431.

57 Dueramae, I.; Ishiyama, T.; Torigaki, A.; Nakano, S.; Sasaki, K.; Kita, R.; Shinyashiki, N.; Yagihara, S.; Katsumoto, Y.; Yoneyama, M. Separation of micro-brownian motion and side-group rotational motion for poly(*n*-isopropylacrylamide) in 1,4-dioxane studied by dielectric relaxation spectroscopy. *Macromolecules* **2023**, *56*, 4041−4048.

https://doi.org/10.1007/s10118-026-3758-7